Production of pions and light fragments at large angles in high-energy nuclear collisions

S. Nagamiya, M.-C. Lemaire,* E. Moeller,† S. Schnetzer, G. Shapiro, H. Steiner, and I. Tanihata‡
Lawrence Berkeley Laboratory and Department of Physics, University of California, Berkeley, California 94720
(Received 9 March 1981)

Inclusive cross sections for production of π^+, π^-, p, d, ^{3}H, ^{3}He, and ^{4}He have been measured at laboratory angles from 10° to 145° in nuclear collisions of Ne + NaF, Ne + Cu, and Ne + Pb at 400 MeV/nucleon, C + C, C + Pb, Ne + NaF, Ne + Cu, Ne + Pb, Ar + KCl, and Ar + Pb at 800 MeV/nucleon, and Ne + NaF and Ne + Pb at 2.1 GeV/nucleon. The production of light fragments in proton induced collisions at beam energies of 800 MeV and 2.1 GeV has also been measured in order to allow us to compare these processes. For equal-mass nuclear collisions the total integrated yields of nuclear charges are well explained by a simple participant-spectator model. For 800 MeV/nucleon beams the energy spectra of protons at c.m. 90° are characterized by a "shoulder-arm" type of spectrum shape with an exponential falloff at high energies, whereas those of pions are of a simple exponential type. The inverse of the exponential slope, E_0, for protons is systematically larger than that for pions. This value of E_0 is larger for heavier-mass projectiles and targets. It also increases monotonically with the beam energy. The angular anisotropy of protons is larger than that of pions. The yield ratio of π^- to total nuclear charge goes up with the beam energy, whereas the yields of composite fragments decrease. The ratio of low-energy π^- to π^+, as well as that of ^{3}H to ^{3}He, is larger than the neutron to proton ratio of the system. The spectrum shape of the composite fragments with mass number A is explained very well by the Ath power of the observed proton spectra. The sizes of the interaction region are evaluated from the observed coalescence coefficients. The radius obtained is typically 3—4 fm. The yield ratio of composite fragments to protons strongly depends on the projectile and target masses and the beam energy, but not on the emission angle of the fragments. These results are compared with currently available theoretical models.

[NUCLEAR REACTIONS Ne + NaF, Ne + Cu, Ne + Pb, E/A = 400 MeV/nucleon; C + C, C + Pb, Ne + NaF, Ne + Cu, Ne + Pb, Ar + KCl, Ar + Pb, E/A = 800 MeV/nucleon; Ne + NaF, Ne + Pb, E/A = 2100 MeV/nucleon; p + C, p + NaF, p + KCl, p + Cu, p + Pb, E = 800 MeV; p + C, p + NaF, p + KCl, p + Cu, p + Pb, E = 2100 MeV; measured $\sigma(p,\theta)$ for π^+, π^-, p, d, ^{3}H, ^{3}He, and ^{4}He.]

I. INTRODUCTION

Since 1977 we have been measuring light fragment spectra at large laboratory angles in high-energy nuclear collisions. Although a part of the data has already been published in letter journals,[1–7] we would like here to report systematically all the existing analyzed data. In the present paper we report inclusive spectra only. In the near future we plan to report particle correlation data including two particle correlations and high multiplicity events.

It is, of course, hard to extract the entire picture of high-energy nuclear collisions from inclusive data alone. Nevertheless, inclusive spectra are important in many aspects. In the first place, all basic processes which occur during the collisions are contained in the inclusive process. Therefore, when one

starts to study nuclear collisions by using new beam energies, or by using new projectile and target species, or by measuring new types of produced particles, the first important experimental variables to be measured are the inclusive spectra. These spectra provide the crude but overall features of the reaction mechanisms involved in the new domain. Secondly, the absolute values of inclusive cross sections are relatively easy to measure, and one can compare the data directly with theoretical predictions, since most of the current theories provide absolute cross sections for inclusive spectra only. In the present paper, we first describe what types of new features are observed in nuclear collisions at high energies, and then compare the data with currently available theories.

In nuclear collisions at beam energies above 0.1 GeV/nucleon, the de Broglie wavelength of the incident nucleons is shorter than the typical internucleon separation ($d \sim 1.8$ fm) inside the nucleus. This fact implies that the projectile nucleons can recognize the individuality of nucleons inside the target nucleus. In other words, the individual interactions between nucleons inside the projectile and target are likely to be more important than the interaction through the mean field. Such a situation is characteristic of nuclear collisions at high energies. Consequently, it becomes quite natural to picture a high-energy nuclear collision as a superposition of nucleon-nucleon collisions, as shown in Fig. 1. Under these circumstances nucleons involved in nuclear collisions may be classified into two types; the participant nucleons which interact strongly with each other during the collision, and the spectator nucleons which are not actively involved in any strong nucleon-nucleon collisions. Of course, such a classification is rather arbitrary and crude, but it helps us to define roughly the kinematical domain into which various types of particles are emitted.

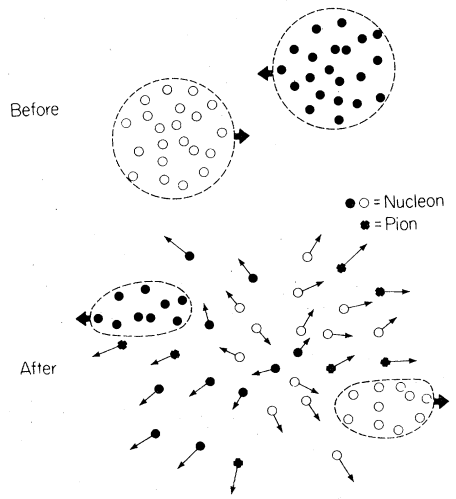

FIG. 1. General features of high-energy nuclear collisions.

In the plane of rapidity $y = \frac{1}{2} \ln[(E + p_{||})/(E - p_{||})]$, and of transverse momentum p_T/mc of an emitted particle, the projectile and target fragments from the spectator nucleons are more likely to be clustered at $(y,p_T/mc) = (y_P,0)$ and $(y_T,0)$, respectively, where y_P and y_T are the projectile and target rapidities. On the other hand, particles emitted from the overlap region between projectile and target, which consists mostly of participant nucleons, are observed over a wide region of rapidity and transverse momentum allowed by the kinematics. These particles are mainly nucleons and pions, since in these nucleon-nucleon collisions the energy transfer involved is much higher than the nucleon binding energies.

In the laboratory frame, projectile fragments tend to be high-energy particles emitted at very small angles, whereas the target fragments are low-energy particles emitted at all angles. Particles from the overlap region are of relatively high energy and are emitted over a wide range of angles. In the present experiment, relatively high-energy light particles π^+, π^-, p, d, ^{3}H, ^{3}He, and ^{4}He have been detected at large laboratory angles. In this respect, our data tend to reflect more of the features of the participant region.

The beams used in the present experiment are Ne at 400 MeV/nucleon, C, Ne, and Ar at 800 MeV/nucleon, and Ne at 2.1 GeV/nucleon. Particles with momenta from a few hundred MeV/c to a few GeV/c were measured by a magnetic spectrometer at angles from 10° to 145°. The projectile mass dependence was studied by using three projectiles, C, Ne, and Ar at 800 MeV/nucleon, and the beam energy dependence was studied with Ne projectiles at three bombarding energies. Targets were (a) of nearly equal mass to the projectile and (b) heavier-mass elements such as Cu and Pb. In order to compare heavy-ion induced collisions with proton induced collisions, we also studied 800 MeV protons and 2.1 GeV protons on various targets.

The present measurements are complementary to many other experimental data obtained at the Bevalac. Papp *et al.*,[8] Anderson *et al.*,[9] Greiner *et al.*,[10] Lindstrom *et al.*,[11] Heckman *et al.*,[12] Westfall *et al.*,[13] and Gazzaly *et al.*[14] have measured

protons and pions at forward angles. Schroeder *et al.*[15] have measured protons and pions at backward angles. These data are primarily related to the study of projectile and target fragmentations. At large laboratory angles, Westfall *et al.*,[16] Gutbrod *et al.*,[17] Gosset *et al.*,[18] Stock *et al.*,[19] and Sandoval *et al.*[20] have reported extensive data for protons, deuterons, and heavier fragments. Our experiment partly shares the same physics interest with these others, but the main difference of our data lies in the energy of the measured particles; namely, we measured relatively high-energy particles while they measured mainly low-energy particles, typically protons less than 200 MeV. Our data for protons cover the energy region from 70 MeV to 2 GeV. With regard to pions, the data of Chiba *et al.*,[21] Nakai *et al.*,[22] Wolf *et al.*,[23] and Benenson *et al.*[24] should be mentioned. Here, low-energy pions below 100 MeV were measured, while we report in this paper relatively high-energy pions, typically from 30 MeV to 1 GeV.

In Sec. II details of the experimental techniques and procedures are described. General remarks about the results are given in Sec. III. In Sec. IV the total inclusive cross sections evaluated from the data are discussed. Several specific features observed in the spectra of protons and pions are presented in Sec. V, and compared with the predictions of theoretical models. Composite fragment emission is described separately for pions and protons in Sec. VI. In Sec. VII the present study is summarized.

II. EXPERIMENTAL TECHNIQUES AND PROCEDURES

A layout of our experimental setup is shown in Fig. 2. A magnetic spectrometer was mounted on a rotatable platform. A total of nine planes of multiwire proportional chambers (MWPC's) placed before and after the spectrometer magnet determined particle trajectories. The momentum, charge, and mass of each particle were determined from three independent experimental variables, time-of-flight between the plastic scintillation counters $G1$ and $G3$, dE/dx of the particle in $G3$ (or $G1$), and the trajectory traced by the MWPC's. In order to cover a wide momentum range (0.3 – 3 GeV/c) we normally took data at two different settings of magnetic field, 10.2 and 3.2 kG.

Beams were accelerated by the Berkeley Bevalac. The size of the beam spot at the target was 4 – 8 mm in both width and height. A typical beam intensity was 10^7 particles/pulse. Each pulse had about a 1 s beam-on period followed by about a 4 – 5 s beam-off period. The beam intensity was monitored by an ionization chamber (IC) and a telescope of three plastic scintillation counters pointed at the target. The position of the beam was monitored by two sets of MWPC's placed upstream and downstream of the target. The targets were mounted on a 10 cm × 10 cm frame. The thickness of each target was typically 1 g/cm^2.

The event trigger used the requirement

$$G = G1*G2*G3 \,. \tag{1}$$

Here we assumed that the efficiency of each of these three counters was close to 100%. The time resolution of the coincidence $G1*G2$ was set at 10 ns while that for $G1*G3$ was 50 ns so that protons with momenta from 100 MeV/c up could be accepted. The MWPC's were not required in the event trigger so that the several efficiencies related to the MWPC's could be evaluated during the off-line analysis.

Data were recorded on-line on magnetic tape by a

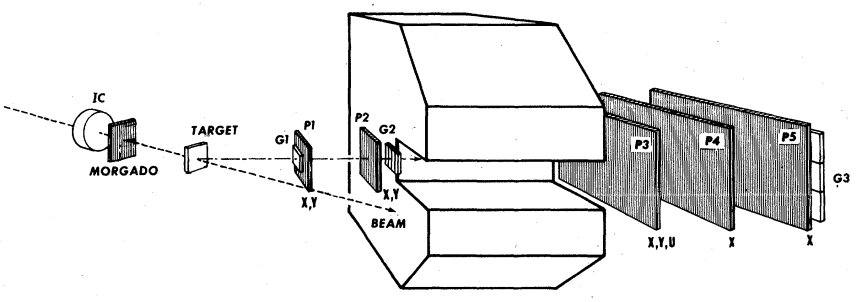

FIG. 2. Layout of the experimental setup.

TABLE I. Beams, targets, detected particles, and the available types of data. An asterisk indicates that the data are partly available.

$E_{\text{beam}}^{\text{lab}}$/nucl (MeV)	Projectile	Target	Detected particles	Data type available Inclusive	TPC[a]	HME[b]
400	Ne	NaF, Cu, Pb	$\pi^{\pm}$, p, d, ^{3}H, ^{3}He	Yes	Yes	*
800	C	C, Pb	π^-, p, d, ^{3}H, ^{3}He	Yes	Yes	*
	Ne	NaF, Cu, Pb	$\pi^{\pm}$, p, d, ^{3}H, ^{3}He	Yes	Yes	Yes
	Ar	KCl, Pb	$\pi^{\pm}$, p, d, ^{3}H, ^{3}He,^{4}He	Yes	Yes	Yes
2100	Ne	NaF, Pb	$\pi^{\pm}$, p, d, ^{3}H, ^{3}He, ^{4}He	Yes	Yes	Yes
800	p	C, NaF, KCl Cu, Pb	π^-, p, d, ^{3}H, ^{3}He	Yes	Yes	No
2100	p	C, NaF, KCl Cu, Pb	$\pi^{\pm}$, p, d, ^{3}H, ^{3}He	Yes	Yes	No

[a]TPC—two-particle correlations.
[b]HME—high-multiplicity events.

PDP 11/20 computer, and then analyzed off line with a CDC 7600 computer. Beams, targets, and the produced particles studied in this experiment are summarized in Table I. The details of each element used in the present experiment as well as the experimental procedures are described in the following subsections.

A. Magnetic spectrometer

As shown in Fig. 2, the magnetic spectrometer consisted of (a) a C magnet, (b) MWPC's, and (c) plastic scintillation counters. The dimensions of these elements are summarized in Table II. The incident angle of a particle into the C magnet, θ_i, was determined by $P1X$ and $P2X$, where the angle $\theta_i = 0$ is defined by a line normal to the detectors $P1$ and $P2$. The outgoing angle, θ_0, from the magnet net was determined by $P3X$ and $P4$. The other five planes of the MWPC's were used to select a good trajectory by requiring various consistency checks. Also, when two or more particles entered the spectrometer, these additional planes were very useful in separating the tracks.

TABLE II. Elements used in the spectrometer.

Element	Dimension	
C magnet	Pole dimension = 33 cm (width) × 61 cm (length) × 15.2 cm (gap)	
Multiwire proportional chambers (MWPC)[a]		
$P1$	64 wires (X) × 64 wires (Y);	1 mm (spacing)
$P2$	64(X) × 64(Y);	2 mm (spacing)
$P3$	192(X) × 192(Y) × 192(U);	2 mm (spacing)
$P4$	256(X);	2 mm (spacing)
$P5$	256(X);	2 mm (spacing)
Plastic scintillators		
$G1$ (1 set)	5.08 cm (width) × 3.81 cm (height) × 0.64 cm (thickness)	
$G2$ (5 sets)	2.54 cm (width) × 7.62 cm (height) × 0.32 cm (thickness)	
$G3$ (3 sets)	55.9 cm (width) × 8.89 cm (height) × 0.95 cm (thickness)	

[a]X indicates vertical wires and Y indicates horizontal wires. The wires indicated by U are tilted by 45° with respect to X and Y.

A three dimensional field map of the C magnet was measured before the installation of the MWPC's. Using the actual magnetic field we performed trajectory calculations for particles with various momenta, and found a simple relation between the particle rigidity (p/Z) and (θ_i and θ_0):

$$\frac{p}{Z} = \frac{B_{\text{eff}}}{\sin\theta_i - \sin\theta_0} \times 21.1 \text{ [(MeV/}c\text{)/ charge]}, \quad (2)$$

where B_{eff} is the effective magnetic field in units of kG. The values of B_{eff} were 10.18 and 3.24 when the magnetic fields at the center of the C magnet were 9.89 and 3.13 kG, respectively. The approximation of Eq. (2) is good to within a 2% accuracy over the whole momentum region measured in the present experiment.

The calibration of the bending angle through the magnet was done by two methods. Firstly, particle tracks at zero magnetic field were measured in order to calibrate the zero bending angle. Secondly, the spectrometer was set at angles $-5°$, $-2.5°$, $0°$, $+2.5°$, and $+5°$, at which settings the bending angle of the primary beam was measured. These calibrations were done occasionally, once or twice per one week run period. From these measurements we found that the bending angle was reliable to within 0.1°, and the absolute rigidity was reliable to within a few percent.

Energy loss (dE/dx) and time-of-flight (TOF) were measured by the plastic scintillation counters $G1$ and $G3$. $G3$ consisted of three counters, each of which was 56 cm long and 8.9 cm wide. The signals from the two ends of each counter were fed to both analog-to-digital converters (ADC's) and time-to-digital converters (TDC's). The digitized ADC outputs of each pair of signals in $G3$ were averaged, after the adjustment of gains, and used to determine the dE/dx of the particle. Also, the average of the TDC outputs was used to obtain the TOF of the particle. In addition, the difference of these TDC outputs was used to determine an approximate position (within a few cm) of the particle in $G3$. This information was used to calibrate the efficiency of the MWPC's, which will be discussed later in Sec. II C.

In order to attain good time resolution of the TOF between $G1$ and $G3$ we fed both $G1$ and $G3$ time signals directly to stop channels of a CAMAC TDC in which a common start was generated by

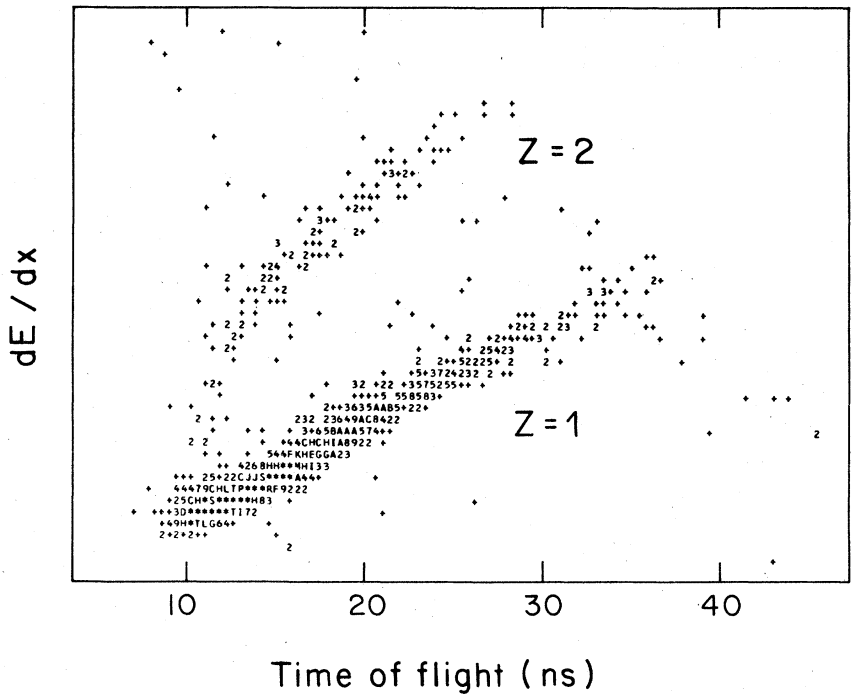

FIG. 3. Scatter plot between time-of-flight (TOF) and dE/dx.

the event-trigger signal. The time resolution of the $G1$-$G3$ TOF was measured by using low-intensity carbon beams at a spectrometer setting of $-2.5°$. Since the timing of the event trigger signal was carefully adjusted so as to be determined by $G1$, the time resolution measured by the $G3$ stop channel (relative to the start event trigger) should in principle be the same as the time resolution measured from the time difference between the two stop channels of $G1$ and $G3$. However, the actual time resolution was 500 ps at FWHM in the former case, while it was 300 ps at FWHM in the latter case. Such an improvement was primarily due to the fact that the time jitters induced by the logic circuits were eliminated when we took the time difference between the $G1$ and $G3$ stop channels.

For a particle with charge Z and velocity βc, the TOF and dE/dx are given by

$$\text{TOF} = d/(\beta c) , \tag{3}$$

$$dE/dx = Z^2 f(\beta) , \tag{4}$$

where d is the distance between $G1$ and $G3$. From Eqs. (3) and (4), the particle charge Z can be determined. Figure 3 shows a scatter plot of TOF and dE/dx for one of the $G3$ counters, from which we selected $Z = 1$ and $Z = 2$ particles. The mixture of $Z = 1$ particles into the $Z = 2$ region due to the Landau tail is negligible ($\lesssim 1\%$).

After the selection of the particle charge, the particle mass was identified from the bending angle and TOF information [see Eqs. (2) and (3)]. Figure 4 shows a scatter plot of $(\tan\theta_i - \tan\theta_0)(180/\pi)$ and TOF for $Z = 1$ particles traversing a 10.2 kG magnetic field, where the former quantity is nearly equal to the bending angle (in units of degrees) for a small bending angle. The choice of $\tan\theta_i$ and $\tan\theta_0$ rather than the bending angle itself was done simply because of the convention of the data analysis, since $\tan\theta_i$ (or $\tan\theta_0$) is the difference in the wire-position readings between two successive MWPC's divided by the distance between these two chambers. We see that p, d, and ^{3}H are very well separated. For the detection of pions and low-energy protons we decreased the magnetic field to 3.2 kG. In this way much clearer separation between pions and protons was obtained. The separation between ^{3}He and ^{4}He was also good.

The momentum resolution for high-energy particles is determined by the wire spacing of the MWPC's, while for low-energy particles the resolution is determined by the multiple Coulomb scattering. The calculated momentum resolution (FWHM) was 10% at 400 MeV/c, 5% at 1000

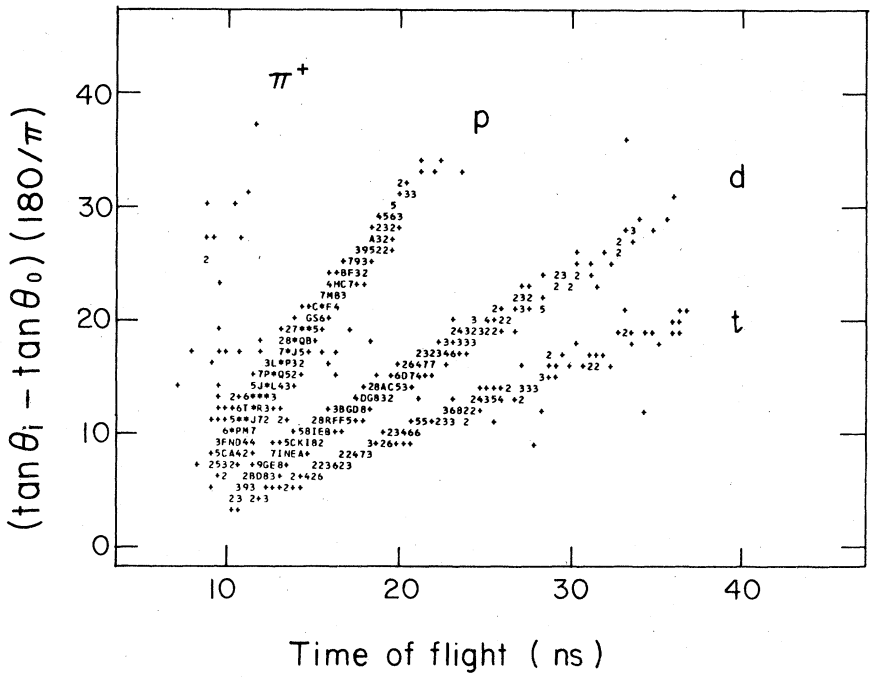

FIG. 4. Scatter plot between time-of-flight (TOF) and $(\tan\theta_i - \tan\theta_0)$ $(180/\pi)$ for $Z = 1$ particles, where the latter quantity is nearly equal to the bending angle in units of degrees when the bending angle is small.

MeV/c, and 10% at 2000 MeV/c. These calculated numbers are comparable to the measured resolution, 8%, 5%, and 14%, respectively, where these experimental numbers were evaluated from the measurements of elastically scattered protons in $p + CH_2$ collisions.

The solid angle of the spectrometer is about 10 msr. The acceptance of the spectrometer as a function of the particle rigidity was calculated by Monte Carlo methods, using the three-dimensional field map. The result is shown in Fig. 5. If the beam spot moves vertically by a few cm, the acceptance decreases by up to $7-8\%$. During the actual data-taking runs we tried to keep the vertical position of the beam within $\pm(2-3)$ mm from the center. In addition, in the data analysis we compared the final results of cross sections with the sample data in which only $G3$ (center) was used, since in the latter case the acceptance is not influenced by modest vertical movement of the beam spot. We confirmed that these sample data were consistent with the final results. The calculated acceptance was experimentally checked by two methods; one by using pp elastic scattering in 800 MeV $p + CH_2$ collisions and the other from the test of the consistency between high ($B_{\text{eff}} = 10.2$ kG) and low ($B_{\text{eff}} = 3.2$ kG) field measurements.

B. Beam monitor

The absolute beam intensity was determined by recording the total charge collected by an ionization chamber (IC) before and after each pulse. At low beam intensities, from 10^3 to 10^6 particles/s, the IC reading was calibrated against the coincidence counts between two plastic scintillation counters (called the B and T counters) inserted in the beam. The actual setup for this calibration run is shown in Fig. 6.

The coincidence between B and T was important, especially for light-ion beams such as protons, since long-lived β-radioactive elements were produced inside the plastic scintillation counters and these elements increased the single counting rate. If we take a coincidence between B and T, however, the coincidence counts are not the true beam flux, because of the scattering of beam particles by the upstream counter (the B counter). The scattering effect was measured by inserting lucite absorbers right after the B counter. The normalized coincidence rate $(B*T)/B$ was measured as a function of the thickness of the lucite absorber and then extrapolated to zero thickness of the B counter. This correction turned out to be about 5%. The IC reading thus calibrated agrees also to within 5% with the calculated values based on the known value of dE/dx in the gas inside the IC.

A monitor telescope (M) placed at 120° with respect to the beam was used to verify that the IC performance did not deteriorate at high beam intensities. The telescope consisted of three plastic scintillation counters, as shown in Fig. 6. Because of its directionality, it detected mainly the fragments from the target. It was designed so that the count ($M1*M2*M3$) was insensitive to the movement of the beam spot at the target. First, the rate M ($=M1*M2*M3$) was measured against ($B*T$) at low beam intensity, and then the IC reading was compared with M at high intensity. The linearity of the IC turned out to be good to within a few percent up to the highest intensity used in the present

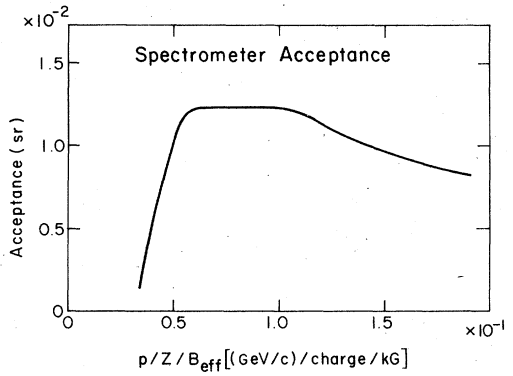

FIG. 5. Acceptance of the spectrometer.

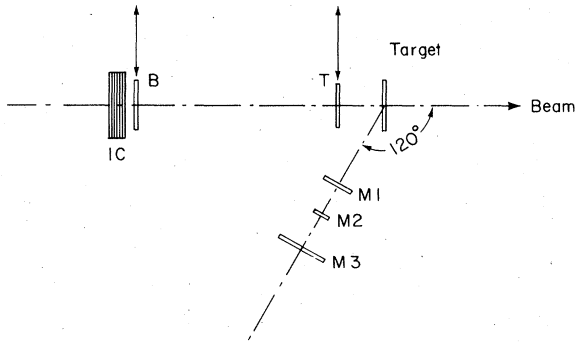

FIG. 6. Beam-intensity monitor system. Both counters B and T were taken out of the beam line after the calibrations of the ion chamber and the monitor telescope ($M1$-$M2$-$M3$).

experiment.

Once the IC and M were calibrated, both could be used to determine the absolute beam flux. Since the target-out/target-in ratio of the coincidence counts M was $\leq 1\%$, we normally used M for the beam intensity determination when the target was in. When the target was out (dummy run), the IC reading was used. The absolute beam flux thus determined was reliable to within $\pm 10\%$.

C. Data taking and off-line data analysis

The electronic circuits were very conventional and will not be discussed here in detail. Three CAMAC crates were controlled by a MBD-11 microprogrammable-branch driver which was coupled to a PDP 11/20 computer. Data were first written on disc and then dumped onto magnetic tape. Signals of TDC's, ADC's, MWPC's, and coincidence registers were recorded in each event. The scaler counts as well as the IC readings were recorded in each beam pulse (with an interval of about 1 s). Normally, histograms of ADC's, TDC's, and MWPC's, as well as two-dimensional scatter plots, were monitored on line on a Tektronix scope display.

The off-line data analysis was done with a CDC 7600 computer. It consisted of the following steps:

(1) *Raw data analysis.* This was done to adjust gains and zero points of ADC and TDC histograms; to select charges of particles from TDC-ADC scatter plots; to obtain good hit patterns of the MWPC's and trace orbits through the spectrometer; to select particle masses from TDC-bending angle scatter plots; and to calculate the momentum of each particle.

(2) *Cross-section evaluation.* This was done to apply necessary corrections to the raw momentum spectrum, such as dead time, MWPC efficiency, spectrometer acceptance, the efficiency of orbit tracing through the MWPC's decay-in-flight correction for pions, etc.; to evaluate multiple scattering effect of particles inside the target or in the spectrometer; and to estimate cross sections and tabulate them.

Several corrections applied in the present experiment are summarized in Table III, in which the type of correction, typical value of the correction, and the associated error are listed. Values of corrections of items (2)—(5) in Table III change from run to run, and were thus calculated in each run. Most of the corrections are self-explanatory.

TABLE III. Corrections and associated errors applied in the present experiment. An asterisk indicates that the correction and associated error are important only for low-momentum region.

Type of correction	Typical correction value		Associated error	
	Proton	Pion	Proton	Pion
(1) Absolute beam intensity	0	0	±10%	±10%
(2) Dead time	20%	20%	±1%	±1%
(3) MWPC efficiency	10%	20%	±5%	±10%
(4) Untraceable good event	2%	10%	±2%	±10%
(5) Beam spread at target	10%	10%	±5%	±5%
(6) Two or more particle hits	0	0	±5%	±5%
(7) Loss due to the dE/dx-TOF scatter plot cut	0	0	±3%	±3%
(8) Loss due to the bending angle-TOF scatter plot cut	0	0	±2%	±2%
(9) Loss due to particle decay in flight	0	*	0	*
(10) Spectrometer acceptance	0	0	±5%	±5%
(11) Target thickness and multiple Coulomb scatterings	*	*	*	*
Overall			±15%	±20%
Other systematic			±15%	±15%
Total			±20%	±25%

Here we describe the MWPC efficiency [item (3)], the orbit-tracing efficiency [item (4)], and the correction for two or more particles entering the spectrometer [item (6)].

The MWPC efficiency was measured by selecting particles with hits in $G1$, $G2$, and $G3$ (center). The particle position at $G3$ (center) was determined from the time difference between two ends of the $G3$ (center) counter, and only particles which geometrically hit all the MWPC's were selected. The efficiency of each MWPC plane was typically 98% but depended on counting rate and particle type. Typically, the efficiency for low-energy protons (<400 MeV) was 99% while that for high-energy protons or pions was 98%. Even with a single plane efficiency of 98%, the total efficiency for nine planes would be down to $\sim 80\%$ if all planes were uncorrelated, and such corrections are not negligible. The efficiencies were evaluated for each of the individual runs and for each type of emitted particle.

The procedure of orbit tracing through the MWPC's was as follows. The hit pattern of particles in each chamber was constructed based on the assumption that if two or more adjacent wires were fired, only one particle was involved. After the construction of the hit patterns of all the MWPC's, the five MWPC's after the magnet ($P3$, $P4$, and $P5$) were first tested to eliminate background hits by imposing two conditions: (a) the horizontal trajectory through $P3X$, $P4$, and $P5$ was a straight line, and (b) the hit patterns within $P3X$, $P3Y$, and $P3U$ (which had wires tilted by 45° with respect to those of $P3X$ and $P3Y$) were mutually consistent. The use of $P3U$ was effective when two or more particles entered the $P3$ chamber. Events satisfying these conditions were then subjected to conditions involving the hit patterns of $P1$ and $P2$. Here we required that (a) an orbit was vertically on a straight line through $P1Y$, $P2Y$, and $P3Y$, (b) the trajectories defined by $P1$ and $P2$ extrapolated to within an area of 1 cm $\times$ 1 cm at the target position, and (c) the horizontal line defined by $P1X$ and $P2X$ intersected the line defined by $P3X$ and $P4$ at approximately the center of the magnet. Such selected orbit(s) were used for the actual determination of the momentum of the particle(s). Some good events were eliminated by imposing these conditions, since the criteria of these conditions were sometimes too strict. By relaxing these criteria we could evaluate the correction for the untraceable good events. This was about 2 – 10 %.

In the case where two or more particles entered the spectrometer, we tried to analyze as many particles as possible. However, unless individual particles hit different $G3$ counters, it was usually not easy to analyze these events because of the incorrect readings of TOF and dE/dx. In addition, the MWPC hits for more than two or three particles entering the spectrometer were not always recorded due to the 32 word limitation of the CAMAC readout module of the MWPC's. These facts have introduced about 5% ambiguity in the absolute values of inclusive cross sections.

Based on the quoted errors in Table III the resultant errors are $\pm 15\%$ for protons and $\pm 20\%$ for pions. However, the proton cross sections taken at $B_{\text{eff}} = 3.24$ kG were occasionally higher than those at $B_{\text{eff}} = 10.18$ kG by a factor up to 1.3 (thus $\pm 15\%$). Taking into account this systematic error of $\pm 15\%$ we conclude the final uncertainties of the absolute cross section values to be $\pm 20\%$ for p, d, ^{3}H, ^{3}He and ^{4}He, and $\pm 25\%$ for pions. Relative values between detected particles are reliable to within $\pm 15\%$ for nuclear fragments and $\pm 20\%$ for pions.

III. TYPICAL FEATURES OF SPECTRA

Since we cannot present here all of the data measured in the present experiment, the complete set of the measured cross sections of p, d, ^{3}H, ^{3}He, ^{4}He, π^+, and π^- together with graphic displays are given separately in Ref. 25. In the present paper we discuss some of the interesting features seen in the data. In this section we present a few examples of the measured cross sections and describe the typical features. In the following three sections we study the total cross sections (in Sec. IV), the proton and pion spectra (in Sec. V), and the composite fragment emission (in Sec. VI).

In Figs. 7 – 11 the momentum spectra of p, d, ^{3}H, ^{3}He, ^{4}He, and π^- in 800 MeV/nucleon Ar + KCl collisions are displayed. In order to compare heavy-ion induced collisions with proton-induced collisions, proton spectra in 800 MeV p + KCl collisions are also presented in Fig. 12. Here the Lorentz-invariant cross sections,

$$\sigma_I = (E/p^2)(d^2\sigma)/(dp\, d\Omega) , \tag{5}$$

are plotted against laboratory momentum.

We first discuss the proton spectra in Ar + KCl as compared with those in p + KCl collisions (Figs. 7 and 12). At forward angles in p + KCl collisions sharp peaks are observed. Here, the pp and pn

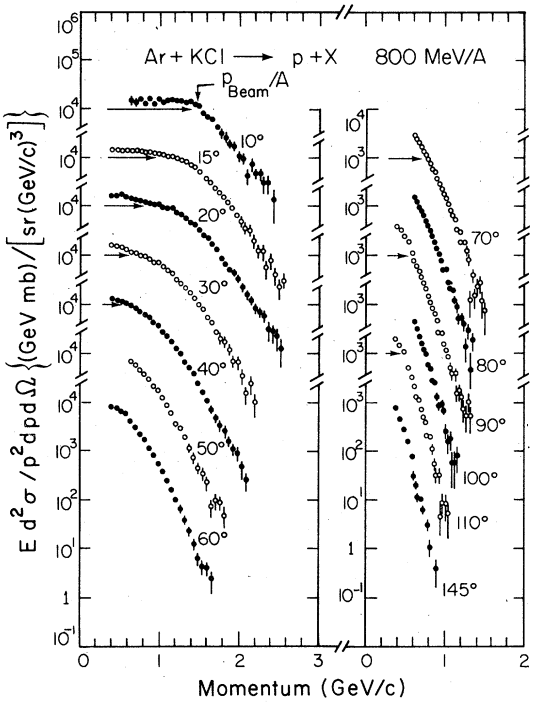

FIG. 7. Inclusive spectra of protons in 800 MeV/nucleon Ar + KCl collisions.

quasielastic scatterings are the important mechanisms.[7] On the other hand, in Ar + KCl collisions such peaks do not show up. The spectra simply vary smoothly with the momenta of the emitted protons. At forward angles in the Ar + KCl case, however, the invariant cross sections at low momenta decrease rather slowly with increasing momenta, while those at high momenta decrease approximately exponentially with a steeper slope. We call such

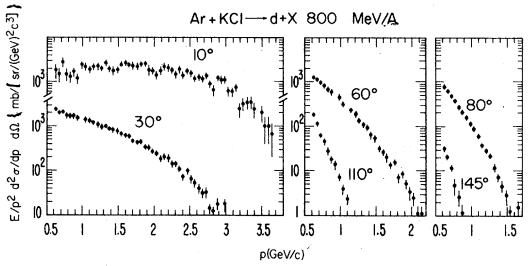

FIG. 8. Inclusive spectra of deuterons in 800 MeV/nucleon Ar + KCl.

a spectrum shape the "shoulder-arm" shape. The turning point between the shoulder and arm is located at a momentum close to the peak observed in p + KCl collisions.

The spectrum in the arm region is interesting. In this region no proton emission is kinematically allowed if the Ar nucleus is a simple assembly of 18 independent stationary protons and 22 neutrons without any mutual interactions. Therefore, the spectrum in this kinematical domain reflects nuclear effects, such as the internal motion of nucleons inside the nucleus, short-range correlation between nucleons,[26–28] or multiple nucleon-nucleon collision effects. These are effects which have long been observed and discussed, particularly from the backward production in proton-nucleus collisions.[15,28–32]

As the laboratory angle increases, the position of the turning point between the shoulder and arm, seen in Ar + KCl, shifts to smaller momentum and the exponential tail becomes steeper. At angles larger than 70° no shoulders are seen within the momentum region measured in the present experiment.

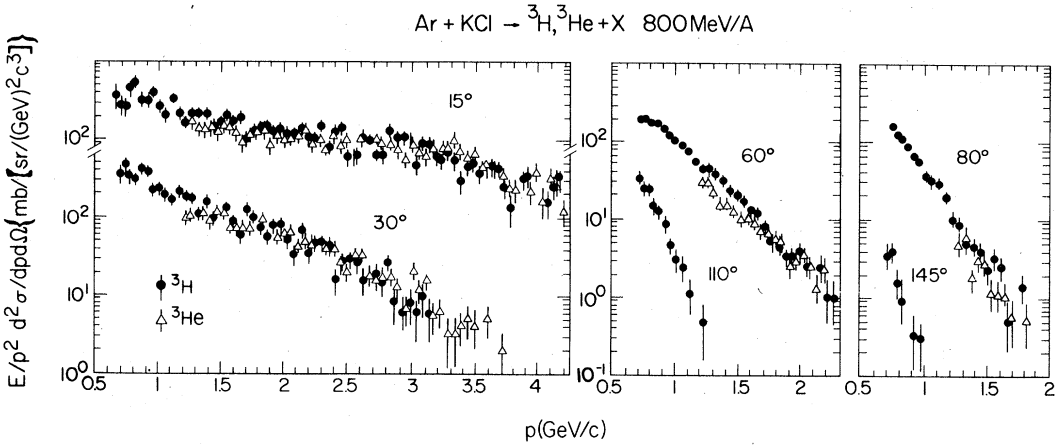

FIG. 9. Inclusive spectra of ^{3}H and ^{3}He in 800 MeV/nucleon Ar + KCl.

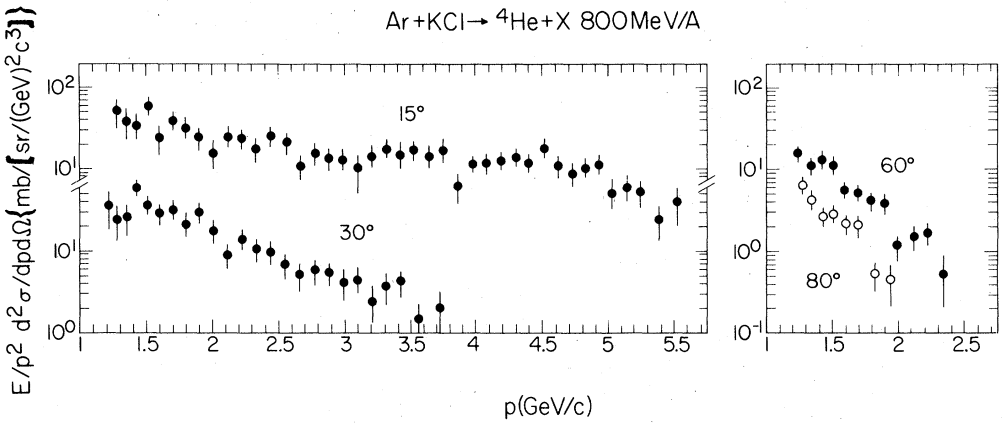

FIG. 10 Inclusive spectra of ^{4}He in 800 MeV/nucleon Ar + KCl.

At angles between 15° and 60° the yields of low-momentum protons ($\sim$400 MeV/c) in the Ar + KCl collisions are about ten times the proton yields in p + KCl collisions. At large angles such as 60°, however, we note that the slope of the proton spectra is less steep for Ar + KCl than for p + KCl. Here, the yield ratio becomes 100 for 1.2 GeV/c protons emitted at 60°. In free nucleon-nucleon collisions the nucleon emission at angles larger than 90° is prohibited by the kinematics. Therefore, the emission of relatively high-momentum protons in

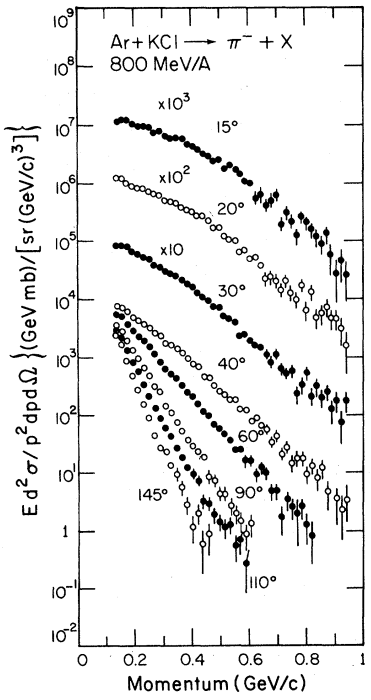

FIG. 11. Inclusive spectra of π^- in 800 MeV/nucleon Ar + KCl collisions.

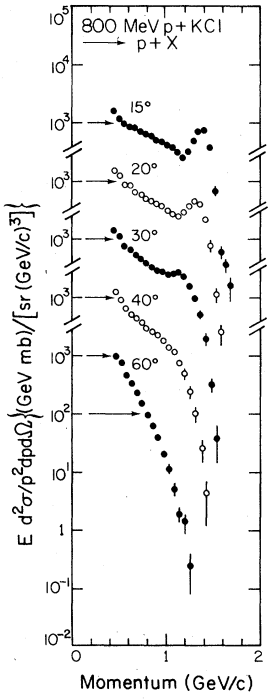

FIG. 12. Inclusive spectra of protons in 800 MeV p + KCl collisions. The momentum of the peak seen at forward angles agrees very well with the expected momentum due to pp or pn quasielastic scattering.

heavy-ion collisions at large angles, especially at backward angles, again supplies interesting information on nuclear effects, similar to that obtainable from a study of high-momentum tails at forward angles.

The above features of the proton spectra seen in Ar + KCl collisions were observed at all of the bombarding energies used in the present experiments and for all combinations of projectiles and targets. Furthermore, we found that low-energy protons (less than a few hundred MeV) are more copiously produced for heavier-mass targets such as Pb than for lighter-mass targets, presumably because of the effects of target fragmentation. Once the projectile mass is fixed, however, the shape of the high-momentum tails at forward angles does not strongly depend on the target mass.

The spectra of composite fragments are shown in Figs. 8—10. Similar to the proton case, the spectra are very smooth functions of fragment momenta. The deuteron spectra at forward angles show a shoulder-arm behavior. The position of the turning point between the shoulder and the arm sits at around 3 GeV/c, which is almost twice the momentum of the turning point observed for protons (see Fig. 7), i.e., at the same velocity as with protons. The ^{3}H, ^{3}He, and ^{4}He spectra have, however, no structure within the momentum regions observed in this experiment. Naively we expect the turning point to be around 4.5 GeV/c for ^{3}H and ^{3}He and to be around 6 GeV/c for ^{4}He. These momenta are larger than the momentum range covered in the present experiment.

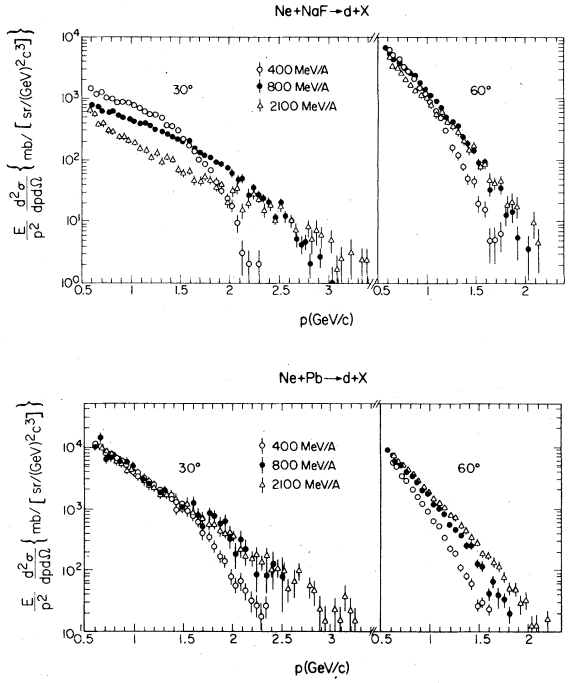

FIG. 13. Deuteron spectra at 30° and 60° in Ne + NaF and Ne + Pb collisions at three different beam energies, 0.4, 0.8, and 2.1 GeV/nucleon.

Examples of the beam energy dependences of the deuteron spectra are shown in Fig. 13 for the Ne

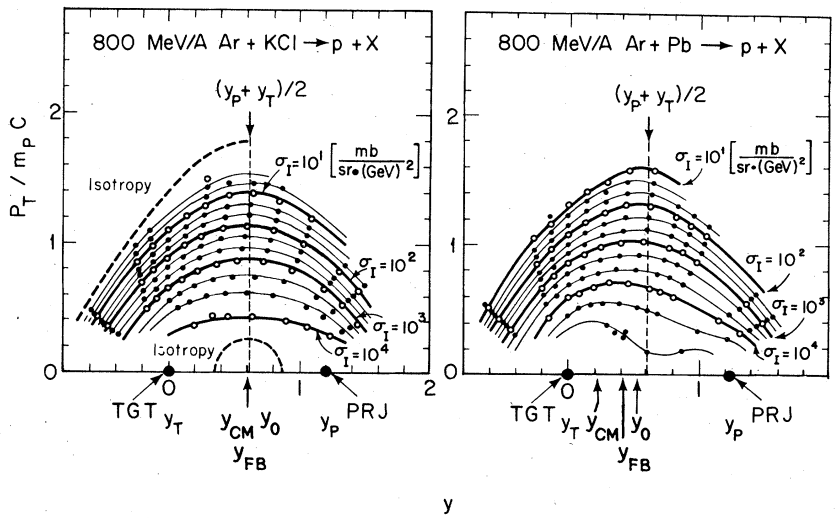

FIG. 14. Contour plots of inclusive proton spectra in the plane of rapidity (y) and normalized transverse momentum (p_T/mc) for 800 MeV/nucleon Ar + KCl and Ar + Pb collisions.

+ NaF and Ne + Pb systems. For the Pb target at $\theta_{lab} = 30°$, the deuteron cross sections are independent of the beam energy at $p_d \leq 1.5$ GeV/c (which corresponds to 260 MeV/nucleon kinetic energy). For the Pb target, not only the cross sections of deuterons but also those for ^{3}H (≤ 2 GeV/c) and protons (≤ 700 MeV/c) at 30° are independent of the beam energy. This confirms the observation reported by Gosset *et al.*[18] in which the spectra of composite fragments, such as ^{3}He, were measured at 30° in Ne + U collisions. For fragments with energies less than 100 MeV/nucleon emitted at 30°, it was found that the spectra are independent of the beam energy. For the NaF target, on the other hand, the 30° spectra have a strong beam energy dependence, as seen from Fig. 13.

In the pion spectra shown in Fig. 11 a clear shoulder-arm shape does not show up at any angle. Instead, the cross sections decrease monotonically with increasing momenta. The decrease of the cross section depends on the angle, being steeper at larger angles. We have also observed that for pions the shape of the spectra and the angular distributions do not depend strongly on the projectile and target masses.

In order to visualize the proton and pion data we display contour plots in Figs. 14 and 15 for both Ar + KCl and Ar + Pb collisions, in the plane of rapidity (y) and normalized transverse momentum (p_T/mc). Two adjacent solid thick curves differ by a factor of 10 in cross section. The projectile and target rapidities are indicated by y_P and y_T, respectively. The line $(y_P + y_T)/2$ corresponds to 90° in the NN (nucleon-nucleon) center-of-mass frame, and $y_{c.m.}$ refers to the rapidity of the c.m. frame of the total projectile plus target system. y_{FB} is the c.m. frame of the participant piece calculated by the straight-line geometry of the participant-spectator model.[33,16]

For proton spectra we expect two peaks at $p_T/m_pc = 0$; one located at $y = y_P$ due to projectile fragmentation and the other at $y = y_T$ due to target fragmentation. When the target mass is larger than the projectile mass, we further expect larger yields at $y = y_T$ than at $y = y_P$. In the small p_T/m_pc region we in fact observe such effects in the data, as shown in Fig. 14.

In the region far from $(y, p_T/m_pc) = (y_P, 0)$ and $(y_T, 0)$, the contributions from the projectile and target are no longer separable. In addition, as we go to higher p_T, the contour lines tend to become symmetrical with respect to the line $y = y_0$. This y_0 is close to $(y_P + y_T)/2$ in the case of Ar + KCl because of the nearly equal masses of the projectile and target. For Ar + Pb the value of y_0 (=0.53) lies between y_{FB} (=0.42) and $(y_P + y_T)/2$ (=0.61).

For the pion spectra shown in Fig. 15, the data cover a much wider kinematical region than the proton data in the plane of y and $p_T/m_\pi c$. Here, the contributions from projectile and target are not separable in any of the kinematical regions. In most of the kinematical region the contour lines are almost symmetrical with respect to the line $y = (y_P + y_T)/2$, although in the Ar + Pb case the symmetry axis tends to shift toward the target rapidity for very low-energy pions.

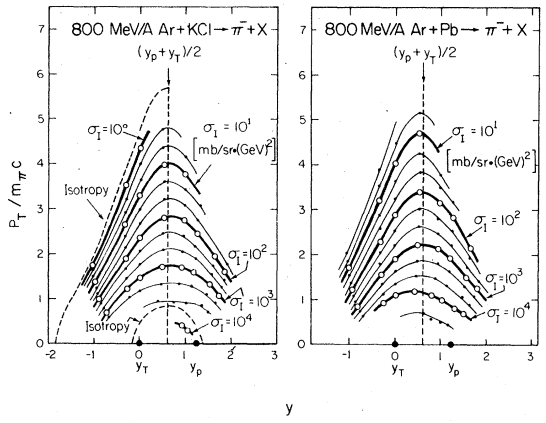

FIG. 15. Contour plots of inclusive π^- spectra in the plane of rapidity (y) and normalized transverse momentum (p_T/mc) for 800 MeV/nucleon Ar + KCl and Ar + Pb collisions.

IV. TOTAL INCLUSIVE CROSS SECTIONS

Before studying the detailed structures of the spectra let us first evaluate the total inclusive cross sections σ_T by integrating σ_I, which is defined by Eq. (5) over all momenta and angles. For this purpose we plot, in Fig. 16, $d^2\sigma/dp\,d\Omega$ as a function of momentum on a linear scale. Each spectrum has a peak at a certain momentum and approaches zero at very small momentum. We assume that $d^2\sigma/dp\,d\Omega = 0$ at $p = 0$. This assumption is well justified, since it is known that σ_I approaches a constant (finite value) at very small momentum.[18,20] In the region of $p \leq 350$ MeV/c no data are available in the present experiment. The contribution to $d\sigma/d\Omega$ from this region is, however, very small at angles smaller than 60°, and a simple extrapolation as shown in Fig. 16 does not induce a large error in

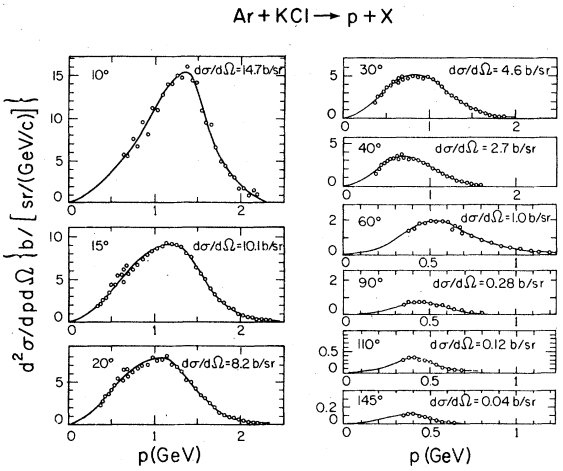

FIG. 16. $d^2\sigma/dp\,d\Omega$ for protons emitted in 800 MeV/nucleon Ar+KCl collisions.

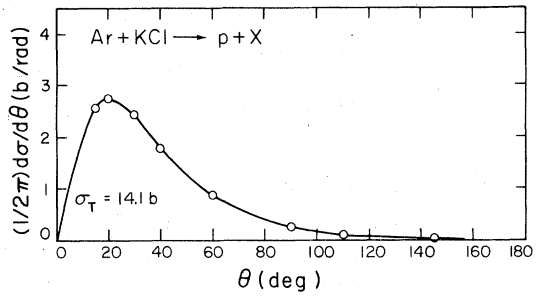

FIG. 17. $d\sigma/d\theta$ plotted as a function of θ for protons emitted in 800 MeV/nucleon Ar+KCl collisions. Integration has been done under the assumption that $d\sigma/d\theta = 0$ at $\theta = 0°$ and 180°. This assumption is reasonable, since $d\sigma/d\Omega$ is expected to have finite values at these angles.

$d\sigma/d\Omega$. At angles larger than 60°, the contribution to $d\sigma/d\Omega$ from the momentum region $p \leq 350$ MeV/c is comparable to that from the $p > 350$ MeV/c region, and the ambiguity in evaluating $d\sigma/d\Omega$ is large. However, since the value of $d\sigma/d\Omega$ itself is very small at these larger angles, such an ambiguity does not cause any significant error in the value of the total cross section σ_T.

Integrations of $d\sigma/d\Omega$ over the angle θ (practically, integrations of $d\sigma/d\theta$ over θ) have been done, in most cases, based on the data taken at angles $15° \leq \theta \leq 145°$. Smooth extrapolations of the data into the angular regions smaller than 15° and larger than 145° have been done in order to evaluate the total yield from $\theta = 0°$ to 180°. An example of the integration is shown in Fig. 17. In Table IV the results of σ_T for p, d, ^{3}H, ^{3}He, ^{4}He, π^+, and π^- are tabulated. In the 10th column of the table are listed the total nuclear charge yields σ_T^Z which have been obtained by

$$\sigma_T^Z = \sum_i \sigma_T^i Z_i \,, \tag{6}$$

where i refers to the type of detected fragment (p, d, ^{3}H, etc.), Z_i is its charge, and σ_T^i is the total inclusive cross section of that fragment. In this section we mainly discuss this σ_T^Z.

In nuclear collisions the geometrical cross section is expressed as

$$\sigma_G = \pi r_0^2 (A_P^{1/3} + A_T^{1/3})^2 \,, \tag{7}$$

where A_P and A_T are the mass numbers of the projectile and target nuclei, respectively. Here, we have assumed that nuclei have sharp radii. If a proton inside the projectile nucleus hits the target, it becomes a participant, otherwise, it remains as a spectator. Under the assumption that the projectile nucleus consists of Z_P independent protons and N_P independent neutrons, the average number of participant protons from the projectile nucleus, which represents the participant charge from the projectile, is given by

$$\langle Z_{\text{proj}}^{\text{parti}} \rangle = Z_P \times (\text{target cross section})/\sigma_G$$
$$= Z_P A_T^{2/3}/(A_P^{1/3} + A_T^{1/3})^2 \,. \tag{8a}$$

Similarly we have

$$\langle Z_{\text{targ}}^{\text{parti}} \rangle = Z_T A_P^{2/3}/(A_P^{1/3} + A_T^{1/3})^2 \,. \tag{8b}$$

The total yield of participant protons, namely the total yield of nuclear charges from the participant region, is therefore given by

$$Y^{\text{parti}}(\text{nuclear charge})$$
$$= (\langle Z_{\text{proj}}^{\text{parti}} \rangle + \langle Z_{\text{targ}}^{\text{parti}} \rangle) \times \sigma_G$$
$$= \pi r_0^2 (Z_P A_T^{2/3} + Z_T A_P^{2/3}) \,. \tag{9}$$

This formula is a natural consequence of the Glauber theory[34] and is also derived by Hüfner *et al.*[35]

Shown in Fig. 18 are the experimental data of total nuclear charge yields σ_T^Z. For equal-mass nuclear collisions (Fig. 18 left) the yield is almost independent of the beam energy, implying that the total yields of nuclear charges are determined mainly

TABLE IV. Total inclusive cross sections for particle emission at large angles.

E_{beam}/A (MeV)	Reaction	Total cross section (b)[a]								
		p	d	^{3}H	^{3}He	α	π^+	π^-	Z^b	$\frac{\pi^-}{Z}$
400	Ne + NaF	3.9	1.2	0.19	0.17	*	0.077	0.086	5.6	1.5×10^{-2}
	Ne + Cu	8.6	3.1	0.66	0.44	*	0.14	*	13.2	*
	Ne + Pb	18.8	8.5	2.2	0.9	*	0.21	0.39	31.3	1.2×10^{-2}
800	C + C	2.2	0.41	0.039	0.034	*	*	0.16	2.7	5.8×10^{-2}
	C + Pb	16.8	7.0	1.6	0.9	*	*	1.17	27.2	4.3×10^{-2}
800	Ne + NaF	5.1	1.12	0.16	0.14	*	0.36	0.41	6.8	6.0×10^{-2}
	Ne + Cu	12.2	3.7	0.74	0.45	*	0.77	0.89	17.8	5.0×10^{-2}
	Ne + Pb	30.5	12.3	3.3	1.4	*	1.37	2.10	49.3	4.1×10^{-2}
800	Ar + KCl	14.1	4.0	0.62	0.52	0.16	1.0	1.4	20.1	7.0×10^{-2}
	Ar + Pb	43.0	18.9	5.0	2.7	1.4	2.2	4.3	76.5	5.6×10^{-2}
2100	Ne + NaF	5.1	0.8	~0.07	~0.05	*	~1.6	1.63	6.0	2.7×10^{-1}
	Ne + Pb	39.7	13.9	2.8	1.5	~0.2	*	10.6	59.8	1.8×10^{-1}
800	p + C	0.33	0.03	0.002	*	*	*	0.008	0.36	2×10^{-2}
	p + NaF	0.52	0.07	0.005	~0.002	*	*	0.014	0.60	2×10^{-2}
	p + KCl	0.86	0.11	0.007	*	*	*	~0.2	0.98	2×10^{-2}
	p + Cu	1.08	~0.21	0.01	*	*	*	*	1.3	*
	p + Pb	1.91	~0.56	0.04	*	*	*	*	2.5	*
2100	p + C	0.26	0.03	0.002	0.002	*	*	0.04	0.30	1.3×10^{-1}
	p + NaF	0.50	0.06	0.005	0.002	*	*	0.08	0.57	1.4×10^{-1}
	p + KCl	0.94	0.12	0.01	0.01	*	*	0.13	1.1	1.2×10^{-1}
	p + Cu	1.15	0.23	0.02	0.01	*	*	0.16	1.4	1.1×10^{-1}
	p + Pb	3.1	0.8	0.09	0.05	*	*	0.34	4.1	0.8×10^{-1}

[a]Typical systematic errors of the absolute values are about ±20% for p and d and ±30% for ^{3}H, ^{3}He, π^+, and π^-. Relative errors are, however, smaller; typically ±10% for d to p, ±15% for ^{3}H to p or for ^{3}He to p, and ±20% for π^- to p. Indicated by * are either "not measured" or "unable to deduce the value because of low statistics." The cross section value with "~" in front of the figure has an error of the order of ±40−50%. [b]Z indicates the total nuclear charge obtained by $p + d + {}^3\mathrm{H} + 2 \times {}^3\mathrm{He} + 2 \times {}^4\mathrm{He}$.

[b]Z indicates the total nuclear charge obtained by $p + d + {}^3\mathrm{H} + 2 \times {}^3\mathrm{He} + 2 \times {}^4\mathrm{He}$.

by the collision geometry. In fact, Eq. (9), which is based on a simple geometrical consideration only, explains very well the absolute values of the data with $r_0 = 1.2$ fm. This value of r_0 is quite reasonable.

For unequal-mass nuclear collisions (Fig. 18 right) we again observe that the yields are roughly explained by Eq. (9). In the Ne + Pb case, however, the yield increases systematically as the beam energy increases. This fact may imply that target fragments from the Pb nucleus get higher excitation energies at higher beam energies, and thus emit more light fragments. This statement may conflict with the concept of limiting fragmentation which has been established for projectile fragmentation studied in light-mass beams.[9–11] However, there is no *a priori* reason to believe that this concept should hold in the fragmentation process from a heavy-mass target such as Pb. In order to release nucleons or light fragments from the target, at least an 8 MeV/nucleon internal energy has to be brought into the system, and this energy is not negligible when the system contains a large number of nucleons. Such a tendency of higher yield at higher

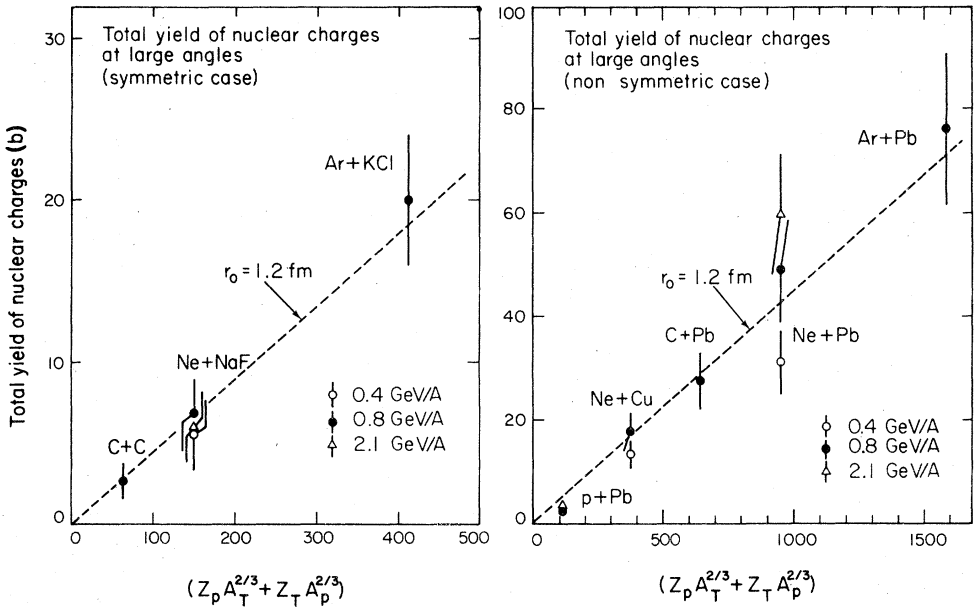

FIG. 18. Total yields of nuclear charges for equal-mass nuclear collisions (left) and unequal-mass nuclear collisions (right), plotted as a function of $Z_P A_T^{2/3} + Z_T A_P^{2/3}$. Data are compared with the predictions given by Eq. (9), which is based on a simple geometrical model.

bombarding energy was also observed by Sandoval *et al.*[20] in their study of Ne+U collisions.

Summarizing the above studies we learn that (a) the total nuclear charge yield σ_T^Z is mainly determined by the collision geometry but not by the collision dynamics, and (b) the particles emitted at large angles, especially those from equal-mass nuclear collisions, are mostly from the participant nucleons.

V. PROTON AND PION SPECTRA

In this section we discuss several features observed in the proton and pion spectra, especially the energy spectra, the projectile and target mass dependences, the angular distributions, the yield ratios of pions to total nuclear charges, the beam-energy dependences, and the π^- to π^+ ratio. Further, in this section, we describe the comparison of the data with theoretical models.

A. Energy spectra at 800 MeV/nucleon

Although relatively high-energy particles emitted at large angles arise mainly from the participant nucleons, the energy spectra at c.m. 90° should be particularly interesting in the study of the reaction mechanism for the participant nucleons, since there the contributions from both projectile and target fragments should be the smallest. We therefore describe first the energy spectra at c.m. 90°.

Shown in Fig. 19 are energy distributions of protons and negative pions at $y = (y_P + y_T)/2$ which corresponds to 90° in the nucleon-nucleon c.m. frame. Here the invariant cross sections are plotted as a function of the kinetic energy E_K^* of protons or π^-. The beam energy was 800 MeV/nucleon for all cases. In general, the spectrum shape does not strongly depend on the projectile and target masses. The shape of the proton spectra approaches an exponential at high energies, while at low energies it substantially deviates from the exponential type. Such a shoulder-arm type of distribution is a typical feature of the proton spectra at 800 MeV/nucleon. For π^-, however, the spectrum shape is almost exponential at all energies.

Let us parametrize the pion spectra, as well as the high-energy proton spectra, by

$$\sigma_I \propto \exp(-E_K^*/E_0) . \tag{10}$$

Then, E_0 is 70—90 MeV for protons and 60—70 MeV for π^-. We observe two features of E_0 from Fig. 19. The first one is that E_0 is systematically

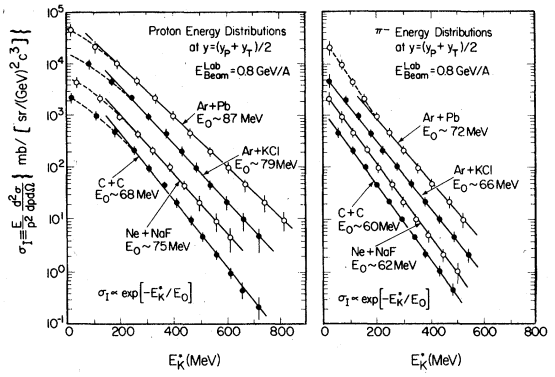

FIG. 19. Proton and π^- energy distributions at $y = (y_P + y_T)/2$ (which corresponds to 90° in the nucleon-nucleon c.m. frame), from several nuclear collisions at 800 MeV/nucleon. E_K^* is the kinetic energy in the nucleon-nucleon c.m. frame. E_0 is the slope factor when the cross sections of high-energy protons or pions are approximated by $\exp(-E_K^*/E_0)$.

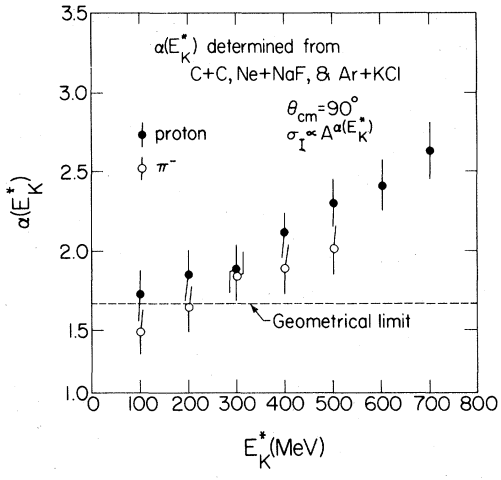

FIG. 20. Projectile and target mass dependences of the proton and π^- cross sections at $\theta_{\text{c.m.}} = 90°$, studied from 800 MeV/nucleon C + C, Ne + NaF, and Ar + KCl collisions. Invariant cross sections (σ_I) are parametrized by $\sigma_I \propto A^{\alpha}$. E_K^* is the kinetic energy in the c.m. frame.

larger for heavier projectile and target combinations; for example, for proton emission, $E_0 = 68$ MeV for C + C but $= 87$ MeV for Ar + Pb. The other feature is that E_0 is systematically larger for protons than for pions. The exponential type of shape, the shoulder-arm type of distribution for protons, together with these two features for E_0, characterize the observed energy spectra at c.m. 90° for 800 MeV/nucleon collisions.

B. Projectile and target mass dependences

We now discuss the projectile and target mass dependences, based on the three almost equal-mass combinations: C + C, Ne + NaF, and Ar + KCl, KCl, at E_{beam}/nucleon = 800 MeV. First, we study the A dependence for particle emission at c.m. 90°. In this case, the cross sections are to a good approximation parametrized by

$$\sigma_I(E_K^*) \propto A^{\alpha(E_K^*)}, \tag{11}$$

where A is the projectile (and target) mass. The observed values of $\alpha(E_K^*)$ are displayed in Fig. 20 for various c.m. kinetic energies E_K^*. If all protons are emitted from direct processes without any multiple collisions, then we expect that the A dependence is determined only by the collision geometry. In this case the expected A dependence of σ_I is given by $A^{5/3}$, since the inclusive yield is proportional to the participant proton number (which is proportional to A) multiplied by the geometrical cross section (which is proportional to $A^{2/3}$). This power dependence can also be easily derived from Eq. (9). We refer to the value of $\alpha(E_K^*) = \frac{5}{3}$ as the geometrical limit. The observed values of $\alpha(E_K^*)$ for low-energy protons are close to this geometrical limit. However, as the proton energy increases, $\alpha(E_K^*)$ increases and reaches 2.6 at $E_K^* = 700$ MeV. Also, the values of $\alpha(E_K^*)$ for π^- are slightly below $\frac{5}{3}$ at low energies but exceed it at high energies. If $\alpha(E_K^*)$ is larger than $\frac{5}{3}$, it implies that the number of nucleons involved in the collisions is larger than expected geometrically. This situation is possible when we have frequent multiple NN collisions. Since high energy particles at c.m. 90° have a large p_T, the observed data imply that high p_T events tend to involve more multiple collisions.

The high-energy protons (or pions) at c.m. 90° correspond to high p_T particles in the midrapidity region between projectile and target. For protons the value of p_T covered by the data shown in Fig. 20 extends up to 1.3 GeV/c. It is interesting to extend this type of A-dependence analysis to various kinematical domains into which particles are emitted. As an example, we studied the A dependence for protons emitted at forward angles, such as 15° in the laboratory frame, in Fig. 21. In this case the value of p_T is relatively small (< 0.6 GeV/c) while the rapidity of the emitted protons extends from 0.5 to 1.5. (Note that $y_P = 1.23$ and $y_T = 0$.) If we

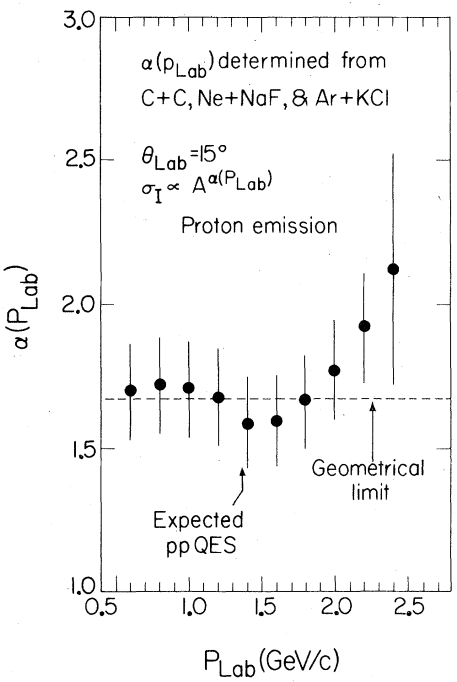

FIG. 21. Projectile and target mass dependence of the proton cross section at $\theta_{lab} = 15°$, studied from 800 MeV/nucleon C + C, Ne + NaF, and Ar + KCl collisions. Invariant cross sections (σ_I) are parametrized by $\sigma_I \propto A^{\alpha}$.

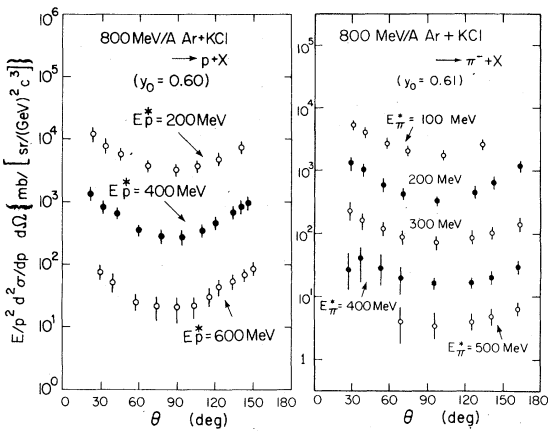

FIG. 22. Angular distributions of protons and π^- in 800 MeV/nucleon Ar + KCl collisions, plotted as a function of the angle in the frame of y_0 (which is close to the nucleon-nucleon c.m. frame). Here, in the y-p_T/mc plane y_0 indicates a line around which the angular distributions of high-energy protons or high-energy pions become symmetrical, as shown in Fig. 14.

parametrize the laboratory cross sections at $\theta_{lab} = 15°$ in the form of $\sigma(p_{lab}) \propto A^{\alpha(p_{lab})}$, then the observed value of $\alpha(p_{lab})$ is very close to $\frac{5}{3}$ in the region of $p_{lab} < 2$ GeV/c. It is larger than $\frac{5}{3}$ only for protons with $p_{lab} > 2$ GeV/c. Therefore, we learn that the A dependence in the small p_T region is almost what is expected by geometry over a wide region of the rapidity.

The expected momentum from pp quasielastic scattering (QES) is 1.37 GeV/c at 15°, as indicated in Fig. 21. Thus we see that the proton emission at $p_{lab} \simeq 2$ GeV/c is far from the nucleon-nucleon kinematical limit in which the nucleus-nucleus collision is regarded as a simple superposition of the nucleon-nucleon collisions. Even in such a high momentum region the observed A dependence is still consistent with the geometrical expectation.[36,37] This fact implies that high-momentum protons in the region of $p_{lab} < 2$ GeV/c are not necessarily emitted through multiple NN collisions. Instead, their production may be more closely attributable to the intrinsic properties of the projectile nucleus, such as Fermi motion or short-range correlations between nucleons.

In the study of high-multiplicity events in Ref. 5 we suggested that the high-momentum tails in the inclusive spectra at forward angles tend to originate from single NN collisions while those at c.m. 90° are mainly multiple NN collisions. This is consistent with the present study of the projectile and target mass dependences.

C. Angular distributions

For Ar + KCl collisions the angular distributions of protons and pions in the c.m. frame are plotted in Fig. 22. For protons strong forward and backward peaking is observed up to very high energies, while for pions the observed anisotropy is less at higher energies. Recently, Chiba *et al.*[21,22] and Wolf *et al.*[23] found that low-energy π^+ ($E_K^* \leq 50$ MeV) have an almost isotropic angular distribution with even a slightly larger yield at around c.m. 90°, while high-energy π^+ at $E_K^* \sim 150$ MeV show forward and backward peaking. Our data are consistent with their high-energy π^+ data. The anisotropy of the pion angular distribution reaches its maximum at pion energies around 150 MeV in the c.m. frame.

In order to study the angular anisotropies in more detail we take

$$R(E_K^*) = 0.5[\sigma_I(\theta_{\text{c.m.}} = 30°) + \sigma_I(\theta_{\text{c.m.}} = 150°)]/\sigma_I(\theta_{\text{c.m.}} = 90°) . \quad (12)$$

The reason we have chosen 30° is that this is the smallest angle covered in the present measurements. As seen in Fig. 23, this ratio for protons monotonically increases with proton energies and reaches a constant value (around 4) at high energies, while that for pions has a peak at around $E_K^* \sim 150$ MeV. Note that we expect $R(E_K^*) = 1$ at $E_K^* = 0$, since the cross section should be independent of angle at $E_K^* = 0$. At beam energies of 800 MeV/nucleon a similar behavior was observed for C + C and Ne + NaF, although in C + C, $R(E_K^*)$ for protons is around 4 at $E_K^* \simeq 200$ MeV and stays constant up to $E_K^* \simeq 600$ MeV.

These features cannot be explained by any conventional theoretical model. We have tested two theoretical models, the firestreak model[38] and the hard-scattering model.[39] However, both models predict anisotropies for high-energy protons which are too large. For high-energy pions the firestreak model predicts too small an anisotropy while the hard-scattering model predicts too large an anisotropy. Neither model predicts the peak for pions at $E_K^* \sim 150$ MeV.

D. Beam energy dependence

In Fig. 24 the energy spectra of protons and negative pions at $\theta_{\text{c.m.}} = 90°$ are plotted for collisions of Ne + NaF at 400, 800, and 2100 MeV/nucleon. At the higher bombarding energies the emitted particles distribute themselves over a wider energy region, and as a result, the inverse slope E_0 increases monotonically with increasing bombarding energies. For the proton spectra the shoulder-arm feature seen at 400 and 800 MeV/nucleon disappears at 2100 MeV/nucleon. For pions the shapes are nearly exponential at all bombarding energies.

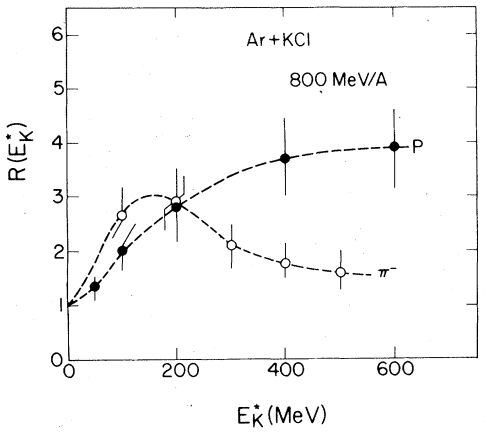

FIG. 23. Angular anisotropies, $R = 0.5\ [\sigma_I(30°) + \sigma_I(150°)]/\sigma_I(90°)$, for protons and π^- emitted in 800 MeV/nucleon Ar + KCl collisions. E_K^* is the kinetic energy in the c.m. frame.

The observed values of E_0 are plotted in Fig. 25 as a function of the available beam energy per nucleon in the c.m. frame. Recently Antonenko *et al.*[40] have measured proton spectra with 3.6 GeV/nucleon ^{4}He and ^{12}C beams and showed that the value of E_0 is about 120 MeV. If we combine their results with ours, it seems that E_0 approaches the limiting value at high energy of about 140 MeV for protons and about 120 MeV for pions. In addition, we should note that, for any beam energy, the value of E_0 is systematically larger for protons than for pions. This point will again we discussed in Sec. V F.

For Ne + NaF collisions the yields $d\sigma/d\Omega$ at c.m. 90° are plotted in Fig. 26 as a function of the available beam energy per nucleon in the c.m. frame. There the proton yield decreases as the beam energy increases. This tendency is opposite to the case of the total proton yields σ_T, which are listed in the 3rd column in Table IV, as σ_T for protons increases with the beam energy. On the other hand, both $d\sigma/d\Omega$ (90°) and σ_T for the π^- yield increase rapidly as a function of the beam energy, and their ratio is almost independent of the beam energy.

These features of the cross sections are consistent with the angular distributions. In Fig. 27 the angular anisotropies $R(E_K^*)$ defined by Eq. (12) are plotted as a function of E_K^*, the kinetic energy in the c.m. frame. For protons the anisotropy is very large at 2.1 GeV/nucleon, especially for higher proton energies. As we decrease the beam energy, the anisotropy becomes smaller. For pions, the anisotropy is small at all beam energies, and $R(E_K^*)$ has less beam-energy dependence than for protons. Such features of the angular distributions in nuclear collisions are at least in qualitative agreement with those observed in *pp* and *pn* collisions. The larger anisotropy means that fewer particles are emitted at 90°. For protons, thus, the 90° yield is expected to be smaller at higher beam energies. For pions, an almost constant ratio of σ_T to $d\sigma/d\Omega$ is expected.

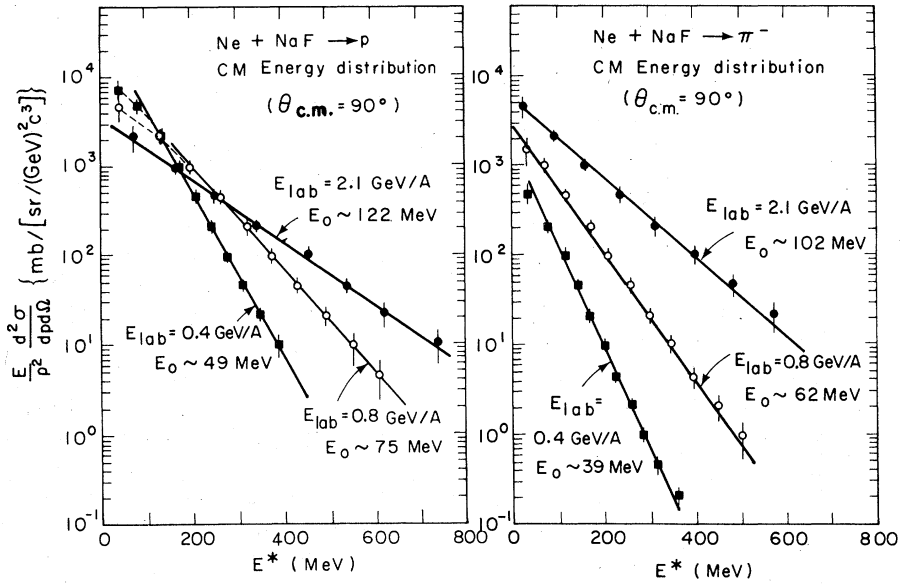

FIG. 24. Proton and π^- energy spectra at $\theta_{c.m.} = 90°$ in Ne + NaF collisions at three beam energies, 0.4, 0.8, and 2.1 GeV/nucleon. E_0 is the slope factor when the cross sections of high-energy protons and pions are parametrized by $\exp(-E_K^*/E_0)$, where E_K^* is the proton (or pion) kinetic energy in the c.m. frame.

The tendencies observed in the ratios of σ_T to $d\sigma/d\Omega$ are therefore consistent with the results of angular anisotropies.

In relation to the angular anisotropy let us ask here what fraction of the total energy flux emerges in the form of charged particles at c.m. 90°. In Table V the experimental results of the quantity $\int E[d^2\sigma/(dEd\Omega)]dE$ at c.m. 90° are listed for π^-, protons, and deuterons in units of (GeV fm²)/sr. Here, E is the kinetic energy in the case of protons and deuterons, whereas it is the kinetic energy plus rest mass in the case of pions. The energy flux at c.m. 90°, E_{flux}, is defined by

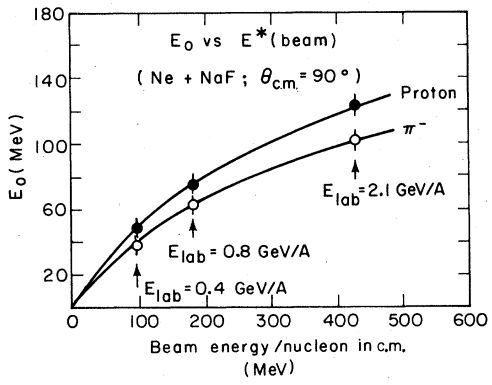

FIG. 25. Observed exponential slope factors E_0 for high-energy protons and π^-, plotted as a function of the available beam energy per nucleon in the c.m. frame. Collisions studied are Ne + NaF.

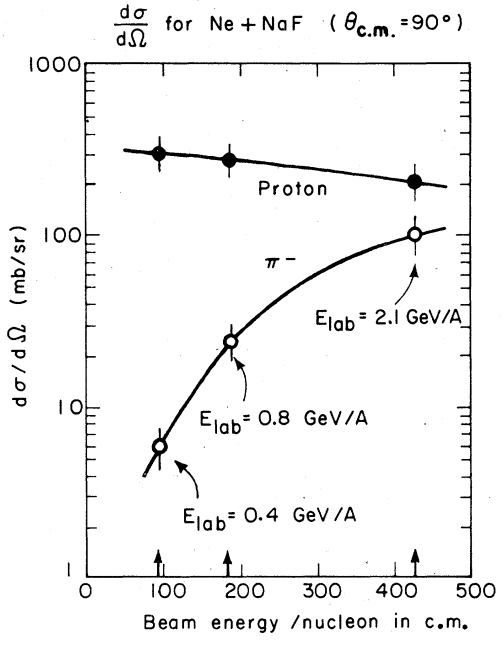

FIG. 26. $d\sigma/d\Omega$ for protons and π^- emitted at c.m. 90° in Ne + NaF collisions. Values are plotted as a function of the available beam energy per nucleon in the c.m. frame.

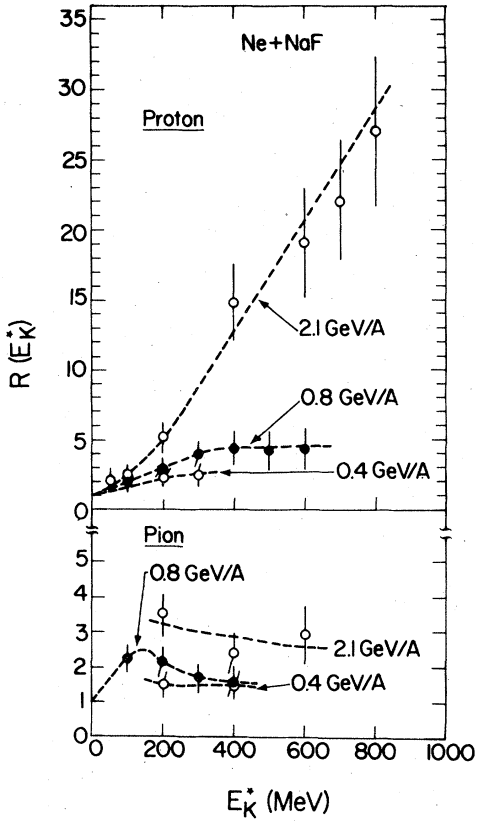

FIG. 27. Angular anisotropies, $R = 0.5[\sigma_I(30°) + \sigma_I(150°)]/\sigma_I(90°)$, for protons and π^- emitted in Ne + NaF collisions at three beam energies, 0.4, 0.8, and 2.1 GeV/nucleon. E_K^* is the kinetic energy in the c.m. frame.

$$E_{\text{flux}} = \int E \frac{d^2\sigma}{dE\, d\Omega} dE/\sigma_0 , \tag{13}$$

where σ_0 is the nucleus-nucleus total cross section. In the 6th column of the table the values of σ_0 are listed in units of fm^2. The numbers listed in the 3rd to 5th columns divided by σ_0 are the observed energy fluxes at c.m. 90°.

In order to compare the results with theoretical expectations, we list in the 7th column of Table V the total energy flux summed over various types of particles which emerges at c.m. 90°, which is $3E_{\text{flux}}(\pi^-) + 2E_{\text{flux}}(\text{proton}) + E_{\text{flux}}(\text{deuteron})$. Assumptions involved here are that $E_{\text{flux}}(\pi^-) = E_{\text{flux}}(\pi^+) = E_{\text{flux}}(\pi^0)$ and $E_{\text{flux}}(\text{proton}) = E_{\text{flux}}(\text{neutron})$. Contributions from nuclear fragments heavier than deuterons are less than 10% of the total energy flux, and thus we neglect them. Also, the contributions from other mesons and leptons are neglected. According to the simple participant-spectator model, if all the kinetic energy brought in by the projectile were to be isotropically emitted in the c.m. frame, the expected total energy flux per unit solid angle, $E_{\text{flux}}^{\text{cal}}$, in the c.m. frame would be given by

$$E_{\text{flux}}^{cal} = (\gamma - 1)m_p c^2 \times [\pi r_0^2 (2A^{5/3})]/(4\pi\sigma_0) , \tag{14}$$

where $(\gamma - 1)m_p c^2$ is the kinetic energy per nucleon in the c.m. frame which was brought in by the projectile and A is the projectile (and target)

TABLE V. Energy fluxes at c.m. 90°. The total energy flux E_{flux} evaluated from the data is listed in the 7th column, which is compared with the calculated value, E_{flux}^{cal}, for an isotropic angular distribution. Errors are typically ±20%.

$E_{\text{beam}}^{\text{lab}}$ / A	Reaction	$\int E[d^2\sigma/(dE d\Omega)]dE$ at c.m. 90° in units of GeV fm^2 /sr			σ_0[c]	Observed[d] E_{flux} at c.m. 90°	Calculated[e] E_{flux} for isotropic distribution	$E_{\text{flux}}^{\text{obs}}/E_{\text{flux}}^{\text{cal}}$
(MeV)		π^-[a]	proton[b]	deuteron[b]	(fm^2)	(MeV/sr)	(MeV/sr)	(%)
400	Ne + NaF	0.13	2.8	0.7	132	51	80	64
	C + C	0.26	1.5	0.27	80	51	103	50
800	Ne + NaF	0.64	3.8	0.8	132	78	153	51
	Ar + KCl	1.7	13.0	2.8	239	142	243	58
2100	Ne + NaF	3.1	3.9	0.4	132	133	358	37

[a]Both pion rest mass and kinetic energy are included.
[b]Only the kinetic energy is included.
[c]Total cross section deduced from Eq. (30) in Sec. VI A 2.
[d]In order to obtain this value we assume that the yields as well as the energy spectra are the same for π^+, π^-, and π^0. We also assume that they are the same for protons and neutrons. Contributions from heavier fragments then deuterons are neglected. Therefore, listed here is $3E_{\text{flux}}(\pi^-) + 2E_{\text{flux}}(p) + E_{\text{flux}}(d)$.
[e] From Eq. (14).

mass number. Here, equal-mass collisions with $N = Z$ are assumed, and this equation is a natural result of Eq. (9). In columns 7 and 8 of Table V the experimental numbers and the above calculated values for E_{flux} are listed, and in the last column the fractions of $E_{\text{flux}}^{\text{obs}}/E_{\text{flux}}^{\text{cal}}$ are listed. As the projectile and target masses increase, more energy flux flows out at c.m. 90°, as seen from three types of collisions at 800 MeV/nucleon. For Ne + NaF at three bombarding energies, we note that the fraction of the available energy flowing out at c.m. 90° decreases with increasing beam energy. The smaller ratio $E_{\text{flux}}^{\text{obs}}/E_{\text{flux}}^{\text{cal}}$ at higher beam energy is consistent with the larger anisotropy of the angular distribution. Furthermore, the larger ratio for a heavier-mass combination between the projectile and target implies that the nucleus becomes less transparent for a heavier-mass system.

When one discusses the beam-energy dependence, the concept of "scaling" should also be mentioned. It was demonstrated by Papp *et al.*[8] that in pion emission at very forward angles the scaling law holds very well; invariant cross sections fall on a universal curve as a function of the Feynman scaling variable $x(=k_{\parallel}^{*}/k_{\max}^{*})$, where $k_{\max}^{*}$ is the maximum c.m. momentum allowed by the kinematics. In addition, Anderson *et al.*[9] showed that the p_T-distribution for projectile fragments is almost independent of the beam energy. It is therefore interesting to test if some scaling law exists for particle emission at large angles. Unfortunately, the present data do not scale with any known scaling variable, such as $x_R(=p_T/p_{\max}^{*})$, $x_R'(=p_T/\sqrt{s})$, or $x_S\{=[(p_T^2+m^2)/s]^{1/2}\}$ proposed in Ref. 41. Instead, we found an empirical scaling law, as plotted in Fig. 28; the cross sections for protons and pions emitted at $\theta_{\text{c.m.}} = 55°$ are, to a good approximation, expressed as

$$\sigma_I = \sigma_0 \exp(-x) , \tag{15}$$

with

$$x = E_K^{*}/\gamma\beta p_0 c \quad \text{for protons}$$
$$= (E_K^{*} + m_\pi c^2)/\gamma\beta p_0 c \quad \text{for pions} , \tag{16}$$

where p_0 is a constant and γ and β are the Lorentz transformation factors which define the nucleon-nucleon c.m. frame relative to the laboratory frame. We choose $\theta = 55°$ in the c.m. because there $P_2(\cos\theta) = 0$ and thus the first-order anisotropy effect vanishes. The best fits, as shown by dotted lines in Fig. 28, have been obtained with $\sigma_0 = 1.8 \times 10^4$ [mbc^3/(sr GeV^2)] and $p_0 = 116$ MeV/c for protons and $\sigma_0 = 3.2 \times 10^4$ [mbc^3/(sr GeV^2)] and

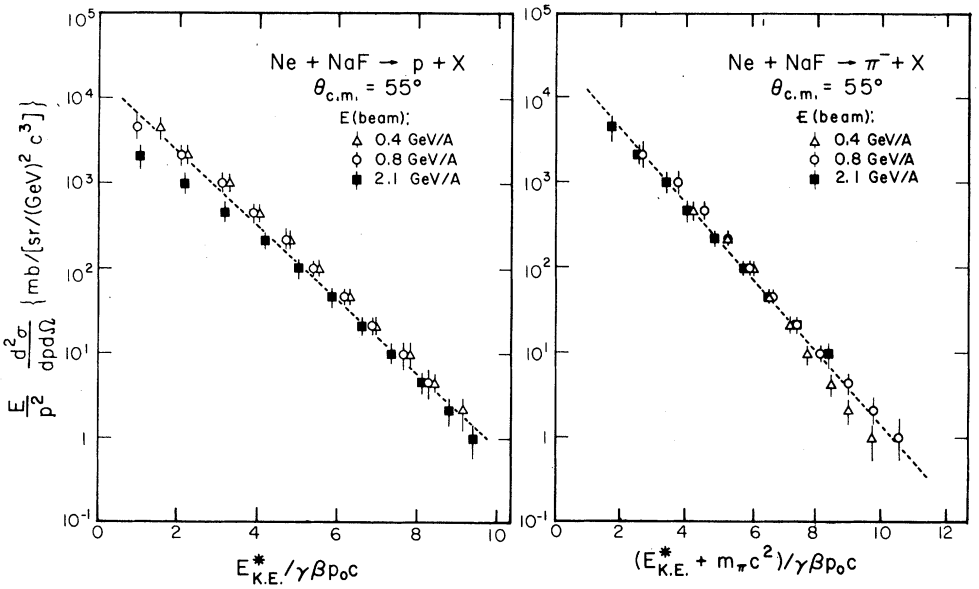

FIG. 28. Empirical scalings for proton and π^- emissions in Ne + NaF collisions. γ and β are the Lorentz transformation coefficients which describe the c.m. frame relative to the laboratory frame. Dotted lines in the figure are drawn at $\sigma_0 = 1.8 \times 10^4$ and $p_0 = 116$ MeV/c for protons and $\sigma_0 = 3.2 \times 10^4$ and $p_0 = 95$ MeV/c for pions, where σ_0 and p_0 are parameters given in Eqs. (15) and (16). Units in σ_0 are (mbc^3)/(sr GeV^2).

$p_0 = 95$ MeV/c for pions. The quantity $\gamma\beta m_p c$ is the c.m. momentum per nucleon of the beam (or target), and $\gamma\beta m_p c$ times the fractional momentum, $p_0/m_p c$, is the denominator in Eq. (16). Therefore, this empirical scaling implies that the proton emission and pion production depend upon the c.m. momentum instead of c.m. energy. Of course, the scalings seen in Fig. 28 are still purely empirical at the present stage and we have not been able to associate any deep physical meaning.

As the final subject of the beam-energy dependence, we discuss the π^- to total nuclear charge (Z) ratio listed in the last column of Table IV. So far, this ratio has been extensively studied in streamer chamber experiments, first by Fung *et al.*[42] and more recently by Sandoval *et al.*[43] We plot their results together with our present data in Fig. 29. A common feature seen from all of these results is that the ratio π^-/Z monotonically increases as the beam energy increases. Although the experimental conditions might be different in these measurements, our observed ratios are consistently larger than those observed by Fung *et al.* The discrepancy of the absolute values of our data from the data of Fung *et al.* might be due to the fact that our data are more biased toward the participant region while their results might include both participant and spectator regions. Sandoval *et al.*, on the other hand, studied equal-mass nuclear collisions, Ar + KCl, especially in central collisions by selecting extremely high-multiplicity events. Their results are consistent with our equal-mass cases, Ne + NaF, C + C, and Ar + KCl, as seen in Fig. 29 and Table IV.

Fung *et al.* stated in their paper that the π^-/Z ratio is almost independent of projectile and target masses. However, upon looking at graphs in Fig. 29 it seems that the results are not independent of mass. In our experiment the π^-/Z ratio systematically decreases as the target mass increases, as seen from the comparison between the Ne + NaF and Ne + Pb cases. Naively one would expect that the π^-/Z ratio should increase as the target mass increases, since π^-/N, which is expected to be nearly equal to π^+/Z, would be a constant in any projectile and target combination, and consequently, π^-/Z would be larger than π^-/N (or π^+/Z) for the system with $N > Z$. The observed result is in contrast to such an expectation, and suggests that pion absorption is important.

Empirically the beam-energy dependence and the target-mass dependence of the π^-/Z ratio are, to a good approximation, given by the following formula:

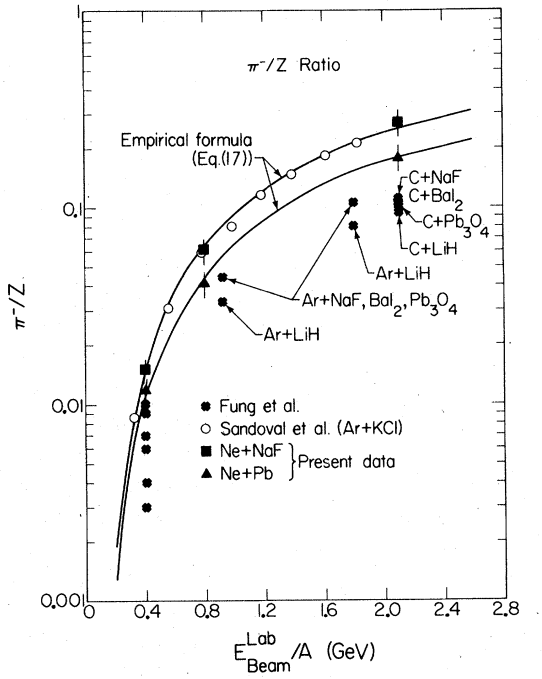

FIG. 29. Ratios of π^-/Z observed in Ne + NaF (black squares) and Ne + Pb (black triangles) collisions, plotted as a function of the laboratory beam energy per nucleon. The same ratios measured by Fung *et al.*[42] (indicated by $\times$) and Sandoval *et al.*[43] (indicated by $\circ$) are also plotted. To a good approximation, the present data as well as the results by Sandoval *et al.* are described by the empirical formula of Eq. (17).

$$(\pi^-/Z) = (A_P/A_T)^{0.15} \exp[-2.15/\beta\gamma^2)] , \quad (17)$$

where β and γ are the familiar Lorentz transformation variables that define the nucleon-nucleon c.m. frame relative to the laboratory frame.

E. Ratio of π^- to π^+

For equal-mass nuclear collisions with equal proton and neutron numbers involved, we expect, to a first order approximation, that both π^- and π^+ yields are the same. However, as pointed out by Benenson *et al.*,[24] for low-energy pions the observed π^- to π^+ ratio at 0° in Ne + NaF collisions is much larger than one, especially at a pion rapidity equal to the beam rapidity. Recent theoretical studies[44,45] indicate that such a large ratio can arise from the Coulomb interaction between pions and positive

nuclear charges. Since the measurements by Benenson *et al.* have been carried out only at 0°, it seemed worthwhile to us to extend such measurements to larger angles.

In Fig. 30 the observed π^- to π^+ ratios in 800 MeV/nucleon Ne + NaF, Ar + KCl, and Ar + Pb collisions are plotted as a function of the pion momentum. In the Ne + NaF case the ratio is larger than unity only in the small momentum region of 30°, while it is close to one at 60° and 90° for all momenta. A similar tendency is also observed for Ar + KCl. These facts imply that the Coulomb effects are anisotropic in the laboratory frame and are stronger at smaller angles. This is consistent with the expectation that most of the nuclear charges are clustered along the beam axis. For Ar + Pb the normally expected π^- to π^+ ratio (without any Coulomb effect) is 1.4—1.5 because of the neutron excess of the system. The observed ratio in the small momentum region at 30° is about 2.5. In the high-momentum region at 90°, however, the observed ratio seems to be less than 1.5.

As to the absolute values of the π^- to π^+ ratio, the recent theoretical papers[44,45] supply the formulas to calculate the numbers. For Ar + KCl at 1.05 GeV/nucleon, the predicted ratio at c.m. 90° at $p_T = 0$ is 2.8 for the fireball geometry and 1.6 for the completely transparent case.[46] By extrapolating our data to $p_T = 0$ at c.m. 90°, we have 2.1 ± 0.3, which is just in between the two extreme cases evaluated by these calculations.

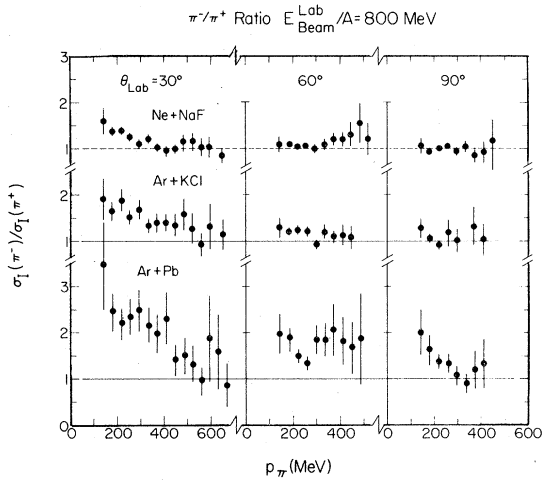

FIG. 30. Ratios of π^- to π^+ studied in 800 MeV/nucleon Ne + NaF, Ar + KCl, and Ar + Pb collisions.

F. Comparison with theoretical models

In this section we compare our proton and pion results with currently available theories. In most theoretical models, the geometrical aspects of the collisions are based on the participant-spectator idea. Since this idea explains reasonably well the total nuclear charge yields at large angles, as studied in Fig. 18, and in addition, since protons are the dominant fragments among the observed nuclear fragments, as seen in Table IV, the absolute integrated yields of protons are explained fairly well by most of the available theoretical models. Differences between models are thus seen mostly in the dynamical aspects of the collisions which are reflected in the energy spectra, angular distributions, pion to nucleon ratios, beam-energy dependences, and composite particle emission. Rather than describe the detailed comparisons of our data with various models we point out in the present paper both the merits and the difficulties associated with each of them.

In the past, two extreme models have been extensively studied; the thermal model and the single *NN* (nucleon-nucleon) collisions model. These two models are based on different and somewhat mutually contradictory physical assumptions, since the thermal model assumes that multiple *NN* collisions are the dominant process so that energy equilibrium is reached among the nucleons involved in the collisions. In terms of the mean free path (λ) and the reaction size (R), the thermal model assumes $\lambda << R$, while the single *NN* collision model assumes $\lambda >> R$. In the energy region of 1 GeV/nucleon it has been shown[7] that $\lambda \sim R$. Therefore, both models are obviously too extreme, and each of these models describes only a very limited aspect of the actual collisions. Despite their obvious shortcomings, however, these models have very frequently been used. Therefore we describe them briefly in the first and the second parts in this section. In the third part we discuss unified models which atttempt to be somewhat more realistic.

In addition to the models described in this paper, hydrodynamical models have extensively been developed during the last few years. These models explain some of the useful features of nuclear collisions and predict interesting possibilities. However, at the present stage direct comparison with our data is not feasible, simply because no calculations on the energy spectra up to high fragment energies are available. With respect to composite fragment production one hydrodynamical calculation has appeared very recently. It will be mentioned later in Sec. VI.

1. *Thermal models*

After the proposal of the nuclear fireball model,[16] several models based on thermodynamics have appeared.[47,48,49] The initial fireball model,[16] in which the participant nucleons are clustered in a single fireball, assumed that the total available energy in the participant piece was completely thermalized. This model has a number of difficulties in reproducing the data. First, the predicted angular distribution is isotropic in the c.m. frame of the fireball, which does not reproduce the observed angular anisotropy seen in Figs. 22, 23, and 27. Secondly, no pion-degrees of freedom are included in this model and thus the pion spectra cannot be explained. As a consequence, the predicted temperature is too high to explain the observed energy spectra; for example, $T = 120$ MeV for 800 MeV/nucleon Ar + KCl which is much higher than the observed slope seen in Fig. 19. Thirdly, the temperature obtained in this model reaches its largest value for equal-mass nuclear collisions, while for unequal-mass collisions the temperature is lower. This again contradicts the observed mass dependence shown in Fig. 19 in which the inverse slope E_0 for Ar + Pb is larger than for Ar + KCl. Therefore, this model is clearly in contradiction to the available experimental facts. The only merit of the initial fireball model is its simplicity and its qualitative explanation of the exponential type of behavior of the proton energy spectra.

The first modification of the fireball model was to include the pion degree of freedom.[50] As a result, the temperature decreased to a value that roughly explains the observed exponential slope. However, two new difficulties arose. As seen in Figs. 24 and 25, the observed proton slope is different from the pion slope, whereas in this model both slopes should be almost equal, reflecting the temperature of the fireball. This is the first difficulty. The second one is that the thermal model predicts a nearly exponential Boltzmann-type spectrum which contradicts the observed shoulder-arm feature seen in Fig. 19.

The firestreak model[51,38] and the two-fireball model[52] were introduced to explain the observed angular anisotropy. These models qualitatively explain a general feature of the large anisotropy for protons and the small anisotropy for pions. In addition, they qualitatively explain the dependence of the inverse slope E_0 on the projectile and target masses. However, two more difficulties arose. the first one is related to the composite particle emission, which will be discussed more in detail in the next section (Sec. VI A 1). The second difficulty is related to the pion energy dependence of the angular distribution. As shown in Figs. 23 and 27 the anisotropy of pion emission in the c.m. frame decreases, above $E_K^* \sim 150$ MeV, as E_K^* increases, while the firestreak model predicts larger anisotropy with larger E_K^*.[38] Furthermore, the two difficulties mentioned in the preceding paragraph; namely, the slope difference between protons and pions and the shoulder-arm feature of the proton spectrum remain unexplained in these models.

The thermal expansion model was introduced later to explain the slope difference between pions and protons.[53] According to this idea the system isentropically explodes after the formation of the initial fireball. During the explosion stage the temperature of the system goes down, and finally, when the particles are emitted, the temperature of the system is significantly lower than that of the initial fireball. Hence, the energy spectrum is the superposition of the thermal spectrum and the explosion flow. Since larger-mass particles are more sensitively affected by the flow velocity, the proton spectrum has a wider energy spread than the pion spectrum. At 800 MeV/nuclon, if we assume that half the available energy goes to the temperature of the final system and the rest goes to the explosive flow, then the observed slope difference between pions and protons is reasonably well explained. Furthermore, the shoulder-arm feature of the proton spectrum as well as the nearly exponential shape of the pion spectrum are well explained. A difficulty with this isentropic expansion model, however, is found in the 2.1 GeV/nucleon data where the proton spectrum has no shoulder-arm structure. Another difficulty of this model lies in the fact that the explosion time is comparable to the thermalization time. Thus, the assumption of this model that the system explodes while staying in thermal equilibrium may not be well justified.

Finally we mention the pion to nuclear-charge ratio discussed in Sec. V D. According to a simple thermal model, which takes into account the pion degree of freedom, the temperature T for equal-mass nuclear collisions is given by[49]

$$E_B^*/A = \tfrac{3}{2}T + 2.28\frac{\rho_0}{\rho}\left[\frac{T}{m_\pi c^2}\right]^{9/2} m_\pi c^2 , \tag{18}$$

where E_B^*/A is the c.m. kinetic energy per nucleon of the incident beam, ρ is the freezeout nucleon density at which particles are actually emitted from the

TABLE VI. Temperature and π^-/Z ratio predicted by a simple thermal model. ρ and T refer to the freezeout density and the temperature, respectively. ρ_0 is the normal nuclear matter density.

$E_{\text{beam}}^{\text{lab}}/A$ (MeV)	$E_{\text{beam}}^{\text{c.m.}}/A$ (MeV)	$\rho/\rho_0 = 0.5$ T (MeV)	π^-/Z	$\rho/\rho_0 = 1$ T (MeV)	π^-/Z	$\rho/\rho_0 = 2$ T (MeV)	π^-/Z	Observed π^-/Z ratio
400	95	56	0.024	59	0.015	61	0.008	0.015 ± 0.003
800	182	83	0.11	91	0.08	99	0.06	0.06 ± 0.01
2100	428	114	0.41	130	0.35	148	0.29	0.27 ± 0.05

fireball, and ρ_0 is the normal nucleon density. For the temperature determined by the above equation, the π^-/Z ratio is given by[48,49]

$$(\pi^-/Z) = 0.46(\rho/\rho_0)(T/m_\pi c^2)^4 \ . \tag{19}$$

In Table VI the calculated temperatures as well as the calculated π^-/Z ratios for various values of ρ are tabulated. In order to reproduce the observed π^-/Z ratio within the framework of the thermal model, we have to take a very large value of the freezeout density such as 2.0. If we take such a large value, however, the temperature is too high to explain the observed slope for protons and pions. In addition, such a large value of the freezeout density seems unrealistic. If we use the commonly accepted freezeout density, $\rho/\rho_0 = 0.5-1.0$,[38,49] the calculated π^-/Z ratios are $50-100\,\%$ larger than the observed values. In this respect, further modifications of the model are needed to explain the observed π^-/Z ratio. For example, it may help to include the transparency of the projectile and target, or the pion absorption effect.

The isentropic expansion model gives a lower temperature than the normal thermal model, but currently this model underestimates the π^-/Z ratio compared with the data, because of the too low temperature.[54] The firestreak model has partly taken into account the transparency effect, but this model still overpredicts the cross sections for pion emission by a factor of 2.[38] All in all the description of these data in terms of presently existing thermal models is not satisfactory.

2. *Single NN collision model*

In the present data several observed features suggest the importance of single *NN* collision processes, namely, the following:

(a) As shown in Fig. 14, y_0, which shows the symmetry axis for high-energy proton angular distributions for Ar + Pb, lies between y_{FB} and $(y_P + y_T)/2$ and closer to the latter, the *NN* c.m. frame.

(b) The turning point between the shoulder and arm of the proton spectrum, as shown in Fig. 7, sits right at the momentum of the *pp* or *pn* quasielastic peak observed in proton-nucleus collisions.

(c) The pion angular distributions exhibit a strong anisotropy at $E_K^* \sim 150$ MeV, as shown in Figs. 23 and 27. This implies that Δ formation via *NN* collisions is likely to be important for pion production at 800 MeV/nucleon.

In addition to these facts, the experimental observations of two-proton correlations[2,6] that proved the existence of quasielastic *pp* or *pn* collisions in C + C, Ne + NaF, and Ar + KCl collisions also suggest the importance of the single *NN* collision processes.

Schmidt and Blankenbecler[55] proposed a single collision model based on an idea similar to the parton model applied in high-energy *pp* collisions. They succeeded in explaining the pion spectra observed by Papp *et al.*[8] at forward angles. This idea was later applied by Hatch and Koonin[39] to explain the data at large angles. They assumed that the momentum (p) of each nucleon inside the projectile (or target) was distributed as

$$(p/p_0)/\sinh(p/p_0) \ ,$$

$$\text{with } p_0 = 90 \text{ MeV}/c \ . \tag{20}$$

This value of p_0 was taken from Ref. 29. The calculations are successful in explaining the gross features of both the proton and pion spectra at 800

MeV/nucleons: The exponential shapes, the observed slopes, the proton and pion yields, and the slope difference between protons and pions are roughly explained.

However, if we look at these calculations more carefully, we find several problems. First, if we use the nucleon momentum distribution of the form of Eq. (20), the shoulder-arm behavior of the proton spectrum cannot be reproduced; the model gives a simple exponential shape for protons. Secondly, the calculated pion energy spectrum has a peak at around $E_K^* \simeq 100$ MeV, while no such peak is observed in the data. Thirdly, at high energies the model predicts too large angular anisotropies for both protons and pions.

In the calculation by Hatch and Koonin, the assumption of Eq. (20) is necessary in order to reproduce the exponential tail in the observed energy spectrum. In our proton-nucleus reaction data,[7] however, we found that the nucleon momentum distribution inside the nucleus is predominantly a Gaussian shape [$\exp(-p^2/2p_0^2)$] rather than an exponential one. If we use the Gaussian shape, then the spectrum shape of protons at c.m. 90° calculated by the single NN collision model is not exponential at high energies, and it falls off much more rapidly than the data.

Our data on event multiplicities associated with single proton emission[5] further showed that these multiplicities were higher when the p_T of the detected proton was larger. Within the framework of the single NN collision model, the associated multiplicities should not depend on this p_T. Considering these observations, the explanation of the high p_T component of the proton or pion spectrum in terms of a single NN collision model under the assumption of Eq. (20) is quite dubious. As stated in Sec. IV B., it is more reasonable to conclude that the high p_T particles are produced by multiple NN collisions.

With regard to the π^-/Z ratio, let us evaluate it by the single NN collision model, using the Δ-isobar model.[56] For an equal-mass nuclear collision with equal numbers of protons and neutrons it is expected that the ratio of the total integrated yields of pions to nuclear charges from the participant region is given by

$$\left[\frac{\pi^-}{N}\right]_{\Delta\text{ model}} = \left[\frac{\pi^+}{Z}\right]_{\Delta\text{model}} = \frac{\frac{5}{6}\sigma_T^{\text{inel}}(pp) + \frac{1}{3}\sigma_T^{\text{inel}}(pn)}{2\times[\sigma_T(pp)+\sigma_T(pn)]} . \quad (21)$$

Here, a simple calculation using Clebsch-Gordan coefficients has been done, and the formula is valid only for the total integrated cross sections. The production rate of π^+, π^0, and π^- is 5:1:0 for $p+p$, 1:4:1 for $p+n$, and 0:1:5 for $n+n$. The combination of pp, pn, and nn collisions in equal-mass nuclear collisions with $N=Z$ is 1:2:1. Therefore, the production rate of π^- is proportional to $(\frac{5}{6})\sigma_T^{\text{inel}}(pp) + 2(\frac{1}{6})\sigma_T^{\text{inel}}(pn)$, which forms the numerator of the above equation. The denominator is the production rate of protons. From $p+p$ and $n+n$ we have two protons, whereas we have only one proton from $p+n$. But, since there is a weight factor of 2 for the $p+n$ combination, the total rate of proton production is proportional to $2[\sigma_T(pp)+\sigma_T(pn)]$. Further assumptions involved in Eq. (21) are: (a) all the inelastic channels are of the $NN\rightarrow N\Delta$ type, namely only a single Δ is excited for one inelastic collision; (b) all the pions are emitted solely from the decay of Δ; (c) there is no absorption of pions during the course of their emission; and (d) $\sigma(pp)=\sigma(pn)$. At 2.1 Gev/nucleon not only Δ but other excited states such as N^* and ρ are produced. Using an empirical pion multiplicity M per inelastic scattering,[57] we approximate the expected (π^-/Z) ratio as

$$\left[\frac{\pi^-}{Z}\right] = M\times\left[\frac{\pi^-}{Z}\right]_{\Delta\text{ model}} , \quad (22)$$

where $M=1$ for 400 MeV and 800 MeV/nucleon and $M=1.44$ (Ref. 57) for 2.1 GeV/nucleon. The predicted values as well as the observed data are compared in Table VII. AT 800 MeV/nucleon the calculated value is about 2.5 times the experimental result, while at 400 and 2100 MeV/nucleon the agreement between theoretical and experimental values is good. It is surprising that the disagreement with the Δ-model predictions is the largest at 800 MeV/nucleon, since it is there that the production cross section of Δ is large. Thus, it is likely that some of the assumptions used in deriving Eq. (21) are not appropriate.

3. *Unified models*

As pointed out earlier, both the thermal and the single NN collision models are too extreme. However, before rejecting them completely we examine attempts at formulating theoretical models which include some features of each. Pirner and Schurmann[58] tried to apply transport theory (the Fokker-Planck equation) to nuclear collisions to describe

TABLE VII. π^-/Z ratio predicted by the single NN collision model using the Δ-isobar model.

E_{beam}^{lab}/A (MeV)	$\sigma_T(pp)$ (mb)	$\sigma_T^{\text{inel}}(pp)$ (mb)	$\sigma_T(pn)$ (mb)	$\sigma_T^{\text{inel}}(pn)$ (mb)	M	π^-/Z calculated	π^-/Z data
400	24.9	1.77	33.3	0.97	1	0.015	0.015 ± 0.003
800	46.3	22.8	34.3	13.5	1	0.15	0.06 ± 0.01
2100	42.3	24.7	40.1	30.3	1.44	0.27	0.27 ± 0.05

both single and multiple NN collision components. The proton data are reasonably well reproduced by this model but the pion data are not. Malfliet[59] developed the sequential-scattering model using the Boltzmann equation to reach a reasonable agreement with the 400 MeV/nucleon data of p, d, ^{3}H, and ^{3}He. Chemtob and Schurmann[60] proposed a direct plus thermal model. The shoulder-arm behavior of the proton spectrum is well reproduced by this model. In these calculations the Gaussian-type momentum distributions of nucleons inside the nucleus were used.

Extensive linear-cascade calculations based on the row-on-row geometry have been reported by Hüfner, Knoll, and Randrup.[35,61,62] Through these calculations they found that, if a nucleon experiences more than two nucleon-nucleon collisions, then the resultant spectrum is, to a good approximation, replaced by a thermal model prediction. By taking into account this conclusion, and by using row-on-row geometry, a theory based entirely on nucleon-nucleon phase space has also been developed.[63,64] With this phase-space theory the proton spectra at 800 MeV/nucleon are very well explained, while the pion spectra, especially their absolute values, are still overestimated by a factor of 2.[64] One inherent problem of the row-on-row model is, however, that it neglects transverse communication between adjacent tubes. Because of this omission, multiple NN collisions after particle emission from the tube are underestimated. For example, the two-proton yields and their target-mass dependence reported in Ref. 7 are not well reproduced. Nevertheless, this linear-cascade approach has the great merit of simplicity compared to the full three-dimensional cascade calculations described below.

The most extensive calculations which could be classified under the term "unified models" are the cascade calculations. So far a number of trials[65–71] involving both classical and quantum mechanical methods have been reported. Among these the calculations by Yariv and Fraenkel[70] and by Cugnon[71] reproduce well, within a factor of 2, our data at 800 MeV/nucleon. Agreement is especially good for protons, but some detailed disagreement is observed for pions. When one compares the data with cascade calculations, however, a difficulty arises in the statistics of the calculated results. Because of this, usual cascade calculations cannot explain very small cross sections. For example, it is not very easy to compare the calculated results with the data in the high p_T region. In general, the unified models reproduce the data better than the two extreme models described in the previous two subsections.

VI. COMPOSITE PARTICLE EMISSION

In this section we discuss two features of the composite fragment spectra. The first one is the spectrum shape of composite fragments as compared with the proton spectrum; it is discussed in Sec. VI A. In Sec. VI B. The yields of composite fragments are compared with those of protons.

A. Spectrum shape

According to a simple phase-space consideration, the probability of forming a deuteron is the greatest when a proton and a neutron are located within an interaction region and have a small relative momentum. Thus we expect

$$P_d(\vec{v} = \vec{v}_d) \propto P_p(\vec{v}_p = \vec{v}_d) \cdot P_n(\vec{v}_n = \vec{v}_d) , \tag{23}$$

where $P(\vec{v})$ is the probability of a particle having the velocity $\vec{v}$. The above relation is called the coalescence model.[72,73,17] In high-energy nuclear collisions the spectra of neutrons can be approximated by those of protons.[74] Thus, we expect for the composite fragment of mass A,

$$E_A(d^3\sigma_A/dp_a^3) = C_A[E_p(d^3\sigma_p/dp_p^3)]^A , \tag{24}$$

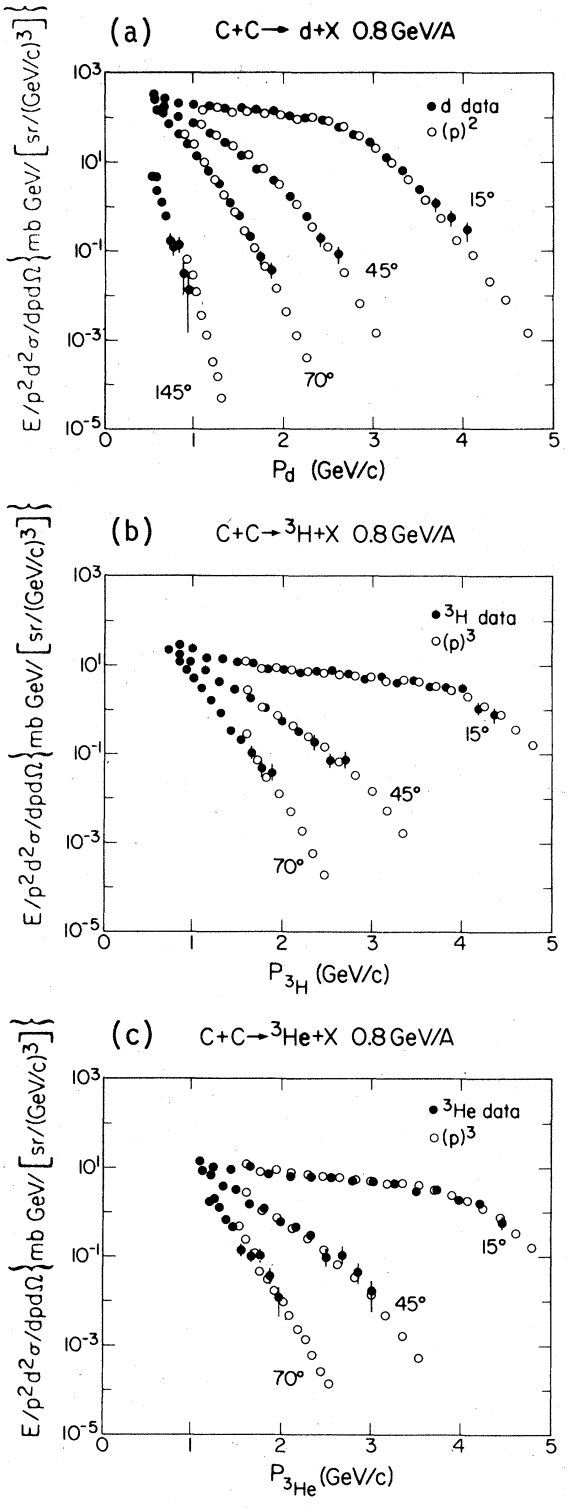

FIG. 31. Spectra of deuterons (a), ^{3}H (b), and ^{3}He (c) in 800 MeV/nucleon C + C collisions, as compared with the squares (for deuterons) and cubes (for ^{3}H and ^{3}He) of the observed proton spectra in the same collisions.

where $p_A = Ap_p$, and C_A is a constant. As an example, the spectra of deuterons are compared with the square of the *observed* proton spectra in Fig. 31(a), and those for ^{3}H, and ^{3}He with the cubes of the proton spectra in Figs. 31(b) and (c). With one normalization constant C_A for each fragment, the relation (22) holds very well at all fragment energies and at all angles.

In Figs. 32 the observed parameters C_A for deuteron emission from the Ne + NaF collisions at three bombarding energies are plotted as a function of the deuteron momentum. As clearly seen from the figure, the value C_A is almost independent of the deuteron momentum and the deuteron emission angle. Further, the value C_A is almost independent of the projectile energy. For all the beam energies and projectile and target combinations studied in the present experiment we found that every d, ^{3}H, ^{3}He, or ^{4}He spectrum is explained very well by Eq. (24) with a parameter C_A which is almost independent of fragment momentum and angle. The observed parameters C_A for various projectile and target combinations are tabulated in Table VIII. As an example, we learn that, for deuteron emission, the parameter C_A is almost independent of the beam energy and depends only on the projectile and target masses.

The good agreement of Eq. (24) with the data raises a fundamental question as to what coalescence is. The original coalescence idea is based on the assumption that, once a composite particle is produced, it never breaks up again into individual nucleons. Therefore, in Eq. (24) the right-hand side

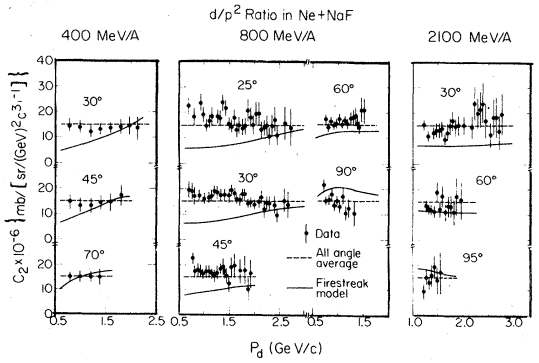

FIG. 32. Ratios of $E_d(d^3\sigma/dp_d^3)/[E_p(d^3\sigma/dp_p^3)]^2$ at $p_d = 2p_p$ for Ne + NaF collisions at three beam energies, 0.4, 0.8, and 2.1 GeV/nucleon. Data are compared with the predictions of the firestreak model.

TABLE VIII. Observed coalescence coefficients C_A (in units of $[(\text{mb/sr})(c^3/(\text{GeV})^2]^{1-A}$) and the radii of the interaction region (in units of fm). Typical errors in C_A are $\pm 20\%$ for d/p^2, $\pm 30\%$ for $^3\text{H}/p^3$, and $\pm 50\%$ for $^3\text{He}/p^3$ and $^4\text{He}/p^4$. The error in R is $\pm 10\%$ in all the cases. The "$\sim$" in front of a figure indicates that the error in C_A is more than a factor of 2, and the symbol "$\approx$" indicates that it is more than a factor of 5. Corresponding errors in R are $\pm 20\%$ for "$\sim$" and $\pm 30\%$ for "$\approx$", respectively.

E_{beam} A (MeV)	Reaction	σ_0[a] (mb)	d/p^2 C_A	d/p^2 R (fm)	$^3\text{H}/p^3$ C_A	$^3\text{H}/p^3$ R (fm)	$^3\text{He}/p^3$ C_A	$^3\text{He}/p^3$ R (fm)	$^4\text{He}/p^4$ C_A	$^4\text{He}/p^4$ R (fm)
400	Ne + NaF	1324	1.4×10^{-5}	3.5	1.3×10^{-10}	3.1	0.8×10^{-10}	3.3		
	Ne + Cu	2051	0.8×10^{-5}	3.7	0.5×10^{-10}	3.2	0.3×10^{-10}	3.4		
	Ne + Pb	3507	4.4×10^{-6}	4.1	1.3×10^{-11}	3.7	0.6×10^{-11}	3.9		
800	C + C	801	3.0×10^{-5}	3.1	0.6×10^{-9}	2.8	0.6×10^{-9}	2.8		
	C + Pb	2973	0.6×10^{-5}	3.9	2.5×10^{-11}	3.5	1.5×10^{-11}	3.5		
800	Ne + NaF	1324	1.6×10^{-5}	3.3	2.1×10^{-10}	2.8	1.6×10^{-10}	3.0		
	Ne + Cu	2051	0.8×10^{-5}	3.7	0.5×10^{-10}	3.2	0.4×10^{-10}	3.3		
	Ne + Pb	3507	0.4×10^{-5}	4.2	1.2×10^{-11}	3.7	0.6×10^{-11}	3.9		
800	Ar + KCl	2390	0.8×10^{-5}	3.5	3.5×10^{-11}	3.2	3.5×10^{-11}	3.2	0.3×10^{-15}	2.8
	Ar + Pb	4556	0.3×10^{-5}	4.3	0.9×10^{-11}	3.6	0.5×10^{-11}	3.7	0.3×10^{-16}	3.0
2100	Ne + NaF	1324	1.4×10^{-5}	3.5	$\sim0.5\times10^{-10}$	$\sim$3.6	$\sim0.5\times10^{-10}$	$\sim$3.6		
	Ne + Pb	3507	0.4×10^{-5}	4.2	$\sim0.6\times10^{-11}$	$\sim$4.2	$\sim0.3\times10^{-11}$	$\sim$4.4		
800	p + C	281	$\sim8\times10^{-5}$	$\sim$3.0	$\approx4\times10^{-9}$	$\approx$2.7	$\approx2\times10^{-9}$	$\approx$3.1		
	p + NaF	406	$\sim5\times10^{-5}$	$\sim$3.3	$\approx10^{-9}$	$\approx$3.2	$\approx10^{-9}$	$\approx$3.2		
	p + KCl	593	$\sim3\times10^{-5}$	$\sim$3.5	$\approx5\times10^{-10}$	$\approx$3.2	$\approx2\times10^{-10}$	$\approx$3.7		
	p + Cu	844	$\sim2\times10^{-5}$	$\sim$3.7	$\approx3\times10^{-10}$	$\approx$3.2	$\approx10^{-10}$	$\approx$3.8		
	p + Pb	1847	$\sim1\times10^{-5}$	$\sim$3.9	$\approx3\times10^{-11}$	$\approx$4.0	$\approx3\times10^{-11}$	$\approx$3.7		
2100	p + C	281	1.0×10^{-4}	2.8	$\approx5\times10^{-9}$	$\approx$2.6	$\approx3\times10^{-9}$	$\approx$2.9		
	p + NaF	406	0.6×10^{-4}	3.1	$\approx10^{-9}$	$\approx$3.2	$\approx10^{-9}$	$\approx$3.2		
	p + KCl	593	0.3×10^{-4}	3.5	$\approx6\times10^{-10}$	$\approx$3.1	$\approx2\times10^{-10}$	$\approx$3.7		
	p + Cu	844	0.2×10^{-4}	3.7	$\approx3\times10^{-10}$	$\approx$3.2	$\approx10^{-10}$	$\approx$3.8		
	p + Pb	1847	1.0×10^{-5}	3.9	$\approx4\times10^{-11}$	$\approx$3.8	$\approx2\times10^{-11}$	$\approx$4.0		

[a]Deduced from Eq. (30).

should contain the originally produced proton spectra before the formation of the composite particles. The good agreement of the data between the *observed* composite fragments and the Ath powers of the *observed* protons suggests that a sort of equilibrium exists between the formation and the breakup of the composite fragments: for example, $d \rightleftarrows p + n$.

The beam-energy independence of the parameter C_A may have further implications. First, it implies that the majority of composite fragments are emitted via final-state interactions. It is possible to use the beam energy dependence to study the various production mechanisms; for example, by detecting knockout clusters we can study the preexisting composite clusters inside the projectile or target. So far no evidence of knockout clusters has been found in the data shown in Fig. 32. In what follows further implications seen in Fig. 32 and Table VIII are described.

1. *Thermal model*

According to a simple thermal model the inclusive spectra of composite fragments with mass number A are expressed as

$$d^3\sigma_A/dp_A^3 = \text{const} \times V \exp(-E_A^*/T) , \qquad (25)$$

where V is the volume of the fireball and E_A^* is the total kinetic energy of the fragment in the fireball c.m. frame. If we take $E_A^* = AE_p^*$, then we readily get Eq. (24) with

$$C_A = \text{const}/(\gamma V)^{A-1} , \tag{26}$$

where γ is the Lorentz factor of the emitted particle measured relative to the c.m. frame of the fireball.[76] In the nonrelativistic limit where $\gamma = 1$, C_A is a constant, and hence the simple thermal model is consistent with the coalescence model. However, in the relativistic case the thermal model does not, in general, agree with the coalescence model. In the data shown in Fig. 32 the range of γ covered by this experiment is 1.0—1.3 for 400 MeV/nucleon, 1.0—1.6 for 800 MeV/nucleon, and 1.1—2.0 for 2100 MeV/nucleon. Therefore, within a factor of 2 the power law between deuterons and protons holds for the simple thermal model.

If we extend the thermal model to the firestreak model, then Eq. (24) does not hold at all. In the firestreak model the temperature from tube to tube is different, and each tube contributes independently to the cross section. For simplicity, if the total system consists of two subsets with equal nucleon numbers but with different temperatures T_1 and T_2 then the left-hand side of Eq. (24) is proportional to

$$[\exp(-E_A^*/T_1) + \exp(-E_A^*/T_2)]/2 = [\exp(-AE_p^*/T_1) + \exp(-AE_p^*/T_2)]/2 \quad \text{for } E_A^* = AE_p^* , \tag{27a}$$

while the right-hand side of Eq. (24) is proportional to

$$[[\exp(-E_p^*/T_1) + \exp(-E_p^*/T_2)]/2]^A \neq [\exp(-AE_p^*/T_1 + \exp(-AE_p^*/T_2)]/2 \quad \text{for } T_1 \neq T_2 . \tag{27b}$$

Therefore, Eq. (24) does not hold. In fact, in the firestreak model the predicted value of C_A has a strong dependence on the fragment momentum and angle, as plotted in Fig. 32, and disagrees with the data. As mentioned previously, the thermal model is an extreme simplification of the multipole NN collisions. Thus, the modification of the thermal model into subsystems in which only a very few nucleons are involved does not seem to be appropriate.

2. *Size of the interaction region*

Since C_A is proportional to $(1/V)^{A-1}$, as seen in Eq. (26), Mekjian[49] proposed that the composite particle emission can be used to determine the source size, which we also call the size of the interaction region. As we saw in the previous subsection, the thermal model is not consistent with the coalescence model. But, if we allow an ambiguity of a factor of 2 in the volume (therefore, 20—30% in the radius), the thermal model can still be used to roughly evaluate the source size.

According to Mekjian the volume is given by

$$V = (x!y!e^{E_0/T})^{1/(A-1)} \left[\frac{3h^3}{4\pi \tilde{p}_0{}^3}\right] , \tag{28}$$

where

$$\tilde{p}_0{}^3 = \left[\frac{2^A}{A^3(2S_A+1)}\right]^{1/(A-1)} p_0{}^3 = \left[\frac{2^A}{A^3(2S_A+1)}\right]^{1/(A-1)} \frac{3m\sigma_0}{4\pi} \times \left[x!y!\left[\frac{Z_P+Z_T}{N_P+N_T}\right]^y A^2 C_A\right]^{1/(A-1)} , \tag{29}$$

and p_0 (or sometimes $\tilde{p}_0$) is called the coalescence radius. Here, x and y are the proton and neutron numbers, respectively, in the composite particle ($A = x + y$), E_0 is its ground state binding energy, T is the temperature, S_A is the spin of the composite particle, m is the nucleon mass, σ_0 is the nucleus-nucleus total cross section, Z_P and N_P are the proton and neutron numbers in the projectile, and Z_T and N_T are the proton and neutron numbers in the target.

In the above formula we can replace $\exp(E_0/T)$ by 1 to a good approximation, since $E_0 << T$. Using the empirical formula of σ_0.[77]

$$\sigma_0 = \pi r_0{}^2(A_p{}^{1/3} + A_T{}^{1/3} - \delta)^2 , \quad \text{with } r_0 = 1.29 \text{ fm} , \tag{30}$$

where

$$\delta = 1.0 - 0.028 A_{\min}$$
$$\text{with } A_{\min} = \text{Min}(A_p, A_T)$$
$$= 0 \quad \text{for } A_{\min} > 30 , \tag{31}$$

we can evaluate the volume V from Eq. (28). The radii R of the equivalent spheres ($V = 4\pi R^3/3$) derived from the volume V are plotted in Fig. 33 for 800 MeV/nucleon C, Ne, and Ar beams. Empirically R can be expressed by

$$R = a(A_P^{1/3} + A_T^{1/3}) + b , \tag{32}$$

with $a = 0.24 \pm 0.08$ fm and $b = 2.0 \pm 0.2$ fm for deuterons, b $= 1.6 \pm 0.2$ fm for ^{3}H and ^{3}He, and $b = 1.0 \pm 0.4$ fm for ^{4}He.

For the Ar + Pb system our analysis leads to a value of R ranging from 3.0 to 4.3 fm, depending on the emitted fragment. For this system a pion interferometry experiment performed at 1.8 GeV/nucleon incident energy[78] gives a value of $R = 3.1 \pm 0.9$ fm in an inelastic trigger mode and 4.0 ± 0.8 fm for the central-collision trigger mode. It is worthwhile to note that such different experiments lead to similar dimensions for the size of the interaction region.

We should also note that the value of R deduced from the present analysis is systematically smaller for heavier-mass fragments. Does it mean that the heavier-mass nuclear fragments are emitted from smaller source volumes? The answer to this question is not clear at the present stage, since the radius obtained from Eq. (28) could include both the effects of source radius and fragment radius. In fact, Sato and Yazaki[79] recently derived a simple relation of $p_0^{-1} \propto (R^2 + R_F^2)^{1/2}$, where R is the source radius and R_F is the radius of an emitted fragment.

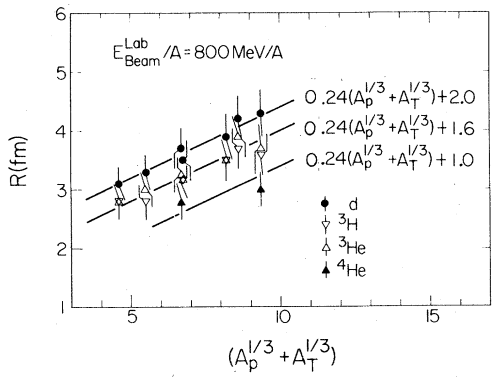

FIG. 33. Radii R of the interaction region deduced from the observed ratios $E_A(d^3\sigma/d^3p_A)$ / $[E_p(d^3\sigma/d^3p_p)]^A$, where $A = d$, ^{3}H, and ^{3}He.

This formula is qualitatively consistent with the present results, as $R_F(d) > R_F(^3\text{H}) \simeq R_F(^3\text{He}) > R_F(^4\text{He})$. However, this formula contains a practical difficulty in fitting our present data, since the value of p_0 has a theoretical upper limit $p_0^{\max}$ in order to satisfy the condition of $R > 0$; according to Sato and Yazaki this $p_0^{\max}$ amounts to 248, 304, and 356 MeV/c for fragments with mass numbers 2, 3, and 4, respectively. The observed values of p_0 are often larger than these values of $p_0^{\max}$, especially for lighter-mass combinations between the projectiles and targets. Clearly, more extended theoretical analysis is required to explain the results shown in Fig. 33.

B. Yield ratio

So far we have discussed the spectrum shape in terms of the power ratio of the cross sections given by Eq. (24). The simple yield ratio

$$R_I(A) = (d\sigma/d\Omega)_A/(d\sigma/d\Omega)_p \tag{33}$$

or

$$R_T(A) = \sigma_T(A)/\sigma_T(p) \tag{34}$$

gives additional information and will be discussed in this section.

In Fig. 34 the ratios $R_I(A)$ are plotted for 800 MeV/nucleon Ar + KCl and Ar + Pb as a function of the laboratory angle. Values of $R_I(A)$ stay almost constant and are equal to $R_T(A)$, except at

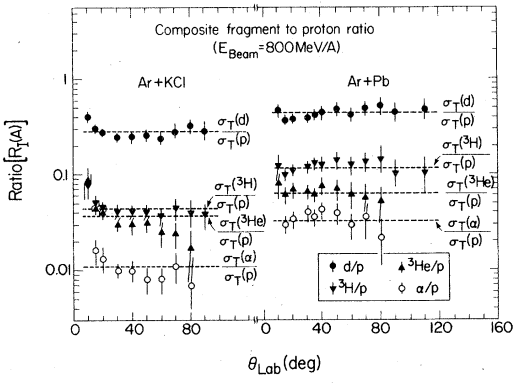

FIG. 34. Ratios $R_I(A) = (d\sigma/d\Omega)_A/(d\sigma/d\Omega)_p$ in 800 MeV/nucleon Ar + KCl and Ar + Pb collisions, plotted as a function of the laboratory angle. Dashed lines in the figure indicate the total integrated ratios, $R_T(A) = \sigma_T(A)/\sigma_T(p)$, where, $A = d$, ^{3}H, and ^{3}He.

forward angles in Ar + KCl collisions, where $R_I(A)$ is slightly larger than $R_T(A)$.

According to the thermal model,[80,49] the yield ratio of composite fragments to protons, $R_T(A)$, is given by

$$R_T(A) = \frac{A^{3/2}}{2^A}(2S_A + 1) \times (\rho_p \cdot \lambda_T{}^3)^{A-1} \left[\frac{N}{Z}\right]^y , \quad (35)$$

where S_A is the spin of the composite particle, ρ_p is the proton "freezeout" or "breakup" density at which the composite fragments are emitted, (N/Z) is the neutron to proton number ratio inside the source, y is the neutron number inside the composite fragment, and λ_T is the thermal wavelength of protons defined by

$$\lambda_T = h/(2\pi m_p T)^{1/2} . \quad (36)$$

Based on Eq. (35) the ^{3}H to ^{3}He ratio should be given by

$$\sigma_T(^3\text{H})/\sigma_T(^3\text{He}) = N/Z . \quad (37)$$

In Fig. 35 the above ratios are plotted as a function of N/Z, where N/Z has been evaluated for the participant region as

$$\frac{N}{Z} = \frac{\langle N \rangle}{\langle Z \rangle} = \frac{N_P A_T{}^{2/3} + N_T A_P{}^{2/3}}{Z_p A_T{}^{2/3} + Z_T A_P{}^{2/3}} . \quad (38)$$

Note that this $\langle N \rangle/\langle Z \rangle$ is almost equal to

$$\frac{N_P + N_T}{Z_P + Z_T} . \quad (39)$$

The observed ratios $\sigma_T(^3\text{H})/\sigma_T(^3\text{He})$ are much larger than N/Z. Empirically, this ratio is expressed approximately by $(N/Z)^2$.

In order to study the large deviation of the ^{3}H to ^{3}He ratio from N/Z we plot in Fig. 36 the ratios

$$[E_A(d^3\sigma_A/dp_A{}^3)]_{A=^3\text{H}}/[E_A(d^3\sigma_A/dp_A{}^3)]_{A=^3\text{He}} , \quad (40)$$

as functions of the fragment momenta for 800 MeV/nucleon Ar + KCl and Ar + Pb collisions. In the case of Ar + Pb the ratio is larger than $(N/Z)_{\text{Pb}}$ and $(N/Z)_{\text{Ar}}$ in the small momentum region, while it is close to unity at very high momentum. such a tendency is commonly observed at all the angles shown in the figure. On the other hand, in the case of Ar + KCl the ratio is much closer to the N/Z ratio of the system, with a slight tendency toward larger ratios in the smaller momentum region.

If we study the total integrated inclusive yield, then the ^{3}H to ^{3}He ratio as well as the π^- to π^+ ratio have almost the same dependence on the N/Z ratio of the system, as seen from Fig. 35. This fact may immediately suggest that the Coulomb effect is important in both cases. However, if we compare the momentum dependence of the ratio for ^{3}H to ^{3}He (Fig. 36) with that for π^- to π^+ (Fig. 30), we notice that the mechanism which causes the deviation of such a ratio from N/Z may not be necessarily the same. For example, in the case of π^- to

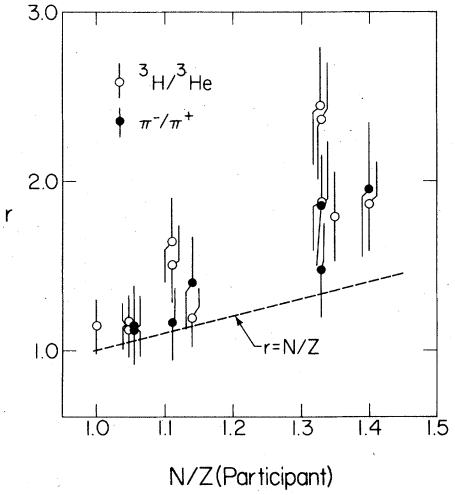

FIG. 35. Ratios $\sigma_T(^3\text{H})/\sigma_T(^3\text{He})$ and $\sigma_T(\pi^-)/\sigma_T(\pi^+)$ plotted as a function of the neutron to proton ratio in the participant region.

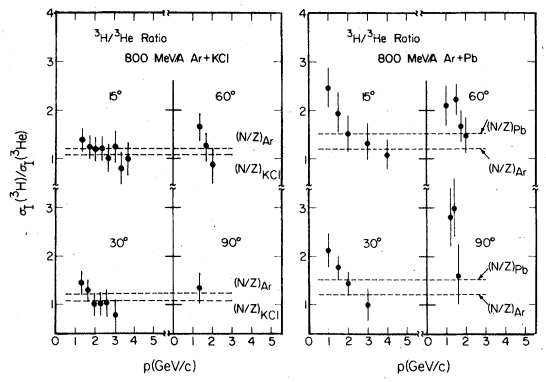

FIG. 36. Ratios of ^{3}H to ^{3}He invariant cross sections in collisions of 800 MeV/nucleon Ar + KCl (left) and Ar + Pb (right), plotted as a function of the laboratory momenta of these fragments.

π^+, a ratio larger than N/Z is observed in the small momentum region at forward angles but not at large angles, while such a large ratio is observed at all angles in the case of ^{3}H to ^{3}He.

For the system with $N/Z > 1$ one would naively expect that a different mechanism might be involved in the case of the ^{3}H to ^{3}He ratio as compared to the π^- to π^+ ratio. The neutron to proton ratio for the nucleons originally produced (in the sense of cascade calculations) would be almost equal to the N/Z ratio of the system. However, some of these nucleons will be combined to form composite fragments before they are actually emitted. Among them the deuteron emission would be the largest. Since deuterons carry equal numbers of protons and neutrons, the remaining neutrons and protons might have a feature that the neutron to proton ratio is larger than the N/Z ratio of the ststem. This idea has been formulated theoretically by Randrup and Koonin[81] and also by Stevenson[82] in order to explain the observed neutron to proton ratios,[75] which are larger than N/Z in Ne + U collisions, especially in the small momentum region. According to these theoretical papers, such a large ratio is expected because deuterons are more easily produced in the low-energy region. A similar argument may hold when one tries to explain the ^{3}H to ^{3}He ratio, since after the formation of deuterons, ^{3}H might be more easily produced than ^{3}He.

The projectile and target mass dependences of the ratio, $R_T(A)$, for 800 MeV/nucleon beams are shown in Fig. 37. The ratio increases as the mass increases. Empirically, the ratio, $R_T(A)$, is proportional to $(A_P + A_T)^\alpha$, where $\alpha = 0.36$ for deuterons and $\alpha = 0.8$ for ^{3}H. The ^{3}He production has no straightforward power law dependence. The observed tendency is more or less understandable. As we increase the mass of the system, it becomes easier for one nucleon to pick up other nucleons to form composite fragments, and the mass dependence is expected to be stronger for three nucleon systems (^{3}H or ^{3}He) than for the two nucleon system (d). The less copious production of ^{3}He than of ^{3}H for heavier-mass systems is simply due to the fact that more neutrons than protons are available in this system. The thermal model formula of Eq. (35) disagrees with the data, since it predicts no projectile and target mass dependence, at least for equal mass nuclear collisions with $N = Z$. Obviously, some important mechanisms, such as the effect of finite nucleon number, are missing in Eq. (35).

The beam energy dependence of the ratios, $R_T(A)$, are shown in Fig. 38. These ratios are

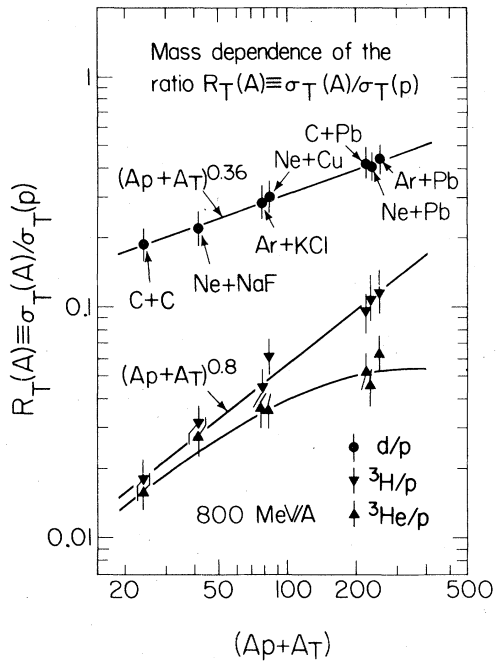

FIG. 37. Ratios $R_T(A) = \sigma_T(A)/\sigma_T(p)$ in several collisions by 800 MeV/nucleon beams, plotted as a function of the sum of the projectile and target masses. Here, $A = d$, ^{3}H, and ^{3}He.

smaller for higher beam energies. The decrease of $R_T(A)$ as a function of the beam energy is more pronounced for Ne + NaF than for Ne + Pb. According to Eq. (35), the beam-energy dependence arises through the terms ρ_p and λ_T, namely from the change of the freezeout density and temperature. Since these two quantities do not strongly depend on the projectile and target masses, the different beam energy dependences of the two targets are not easy to explain by Eq. (35).

Qualitatively, however, the observed behavior in Fig. 38 could be explained as follows: As we increase the beam energy, a larger phase-space volume will be opened up. Since formation of composite fragments is less likely for larger phase-space volumes, we expect smaller ratios of d/p, ^{3}H/p, and so on. Such a tendency is clearly observed for Ne + NaF. In heavier-mass targets such as Pb, slow composite fragments could be produced more copiously because they tend to originate in the target. Since it is expected that the spectra of target fragments do not have strong beam energy dependence, we could expect less beam energy dependence for heavier-mass targets.

The beam energy dependence of the composite

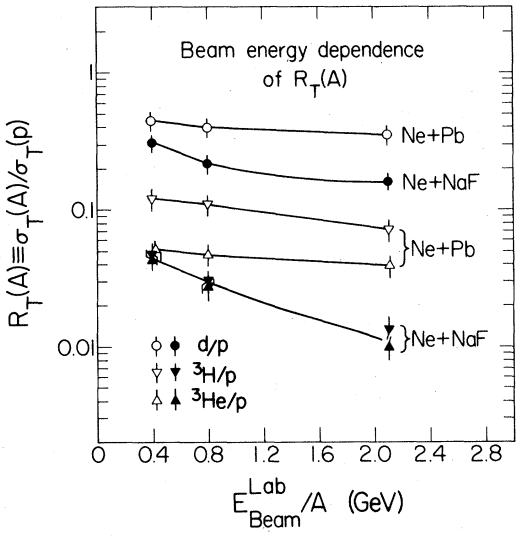

FIG. 38. Beam energy dependences of the ratios $R_T(A) = \sigma_T(A)/\sigma_T(p)$ in Ne + NaF and Ne + Pb collisions. Here, $A = d$, ^{3}H, and ^{3}He.

fragment emission is closely related to the recent work on entropy.[83–85,54] According to Siemens and Kapusta,[83] the observed entropy is much larger than the normally expected value. They evaluated the experimental entropies from theoretical fits of their explosion model to our measured proton and deuteron spectra at c.m. 90°. However, if we evaluate the experimental entropies solely from the observed ratios of deuterons to protons, the resultant values of entropies are somewhat smaller than those reported in Ref. 83.

In Fig. 39 the measured entropies evaluated from

$$\text{entropy} = 3.95 - \ln(N_d/N_p) \tag{41}$$

are plotted as a function of baryon energy per nucleon in the c.m. frame. Data points were obtained from the ratios of $(d\sigma/d\Omega)$ at c.m. 90° and also from the ratios of total cross sections listed in Table IV. At E^{lab}_{beam}/nucleon = 2.1 GeV the value of the horizontal axis, the energy available to the baryon degrees of freedom, is model dependent; there we assumed that half the available energy goes to the baryon degree of freedom.[86] Mishustin *et al.*[84] have recently reported theoretical entropy values which are larger than those obtained by Siemens and Kapusta. At 0.8 and 2.1 GeV/nucleon the theoretical values obtained by Mishustin *et al.* agree reasonably well with the data. Significant disagreement is observed at 400 MeV/nucleon only. Garpman *et al.*[85] have evaluated entropy values in nuclear matter by including several baryonic resonances, and showed that the entropy increases if one takes into account these resonances. At 400 MeV/nucleon their result agrees very well with that of Siemens and Kapusta, because there the baryonic excited states do not play an important role. However, at higher energies such as 2.1 GeV/nucleon their value is even larger than the value calculated

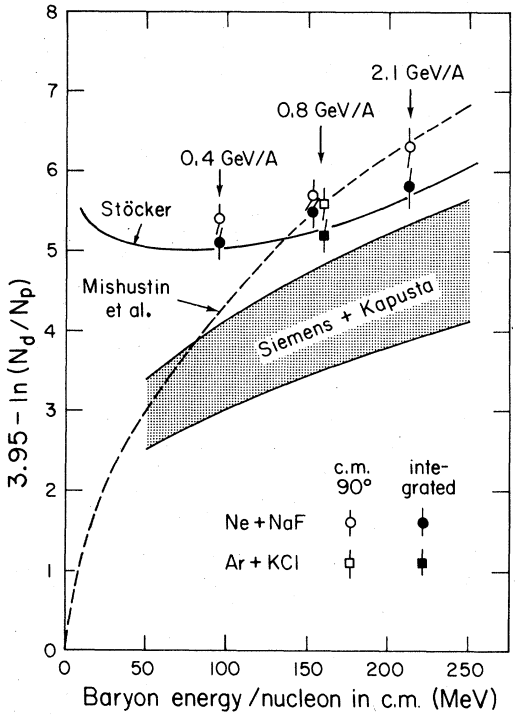

FIG. 39. Observed values of $3.95 - \ln(N_d/N_p)$ in Eq. (41), as compared with the theoretical predictions. In order to directly compare the data with the theoretical predictions reported in Refs. 83 and 84, the horizontal axis must be the energy per nucleon in the c.m. frame for the baryon degrees of freedom. This is nearly equal to the c.m. beam energy per nucleon minus the energy taken out by the pion degrees of freedom, but the value itself is model dependent. For an 800 MeV/nucleon beam this baryon energy per nucleon (c.m.) is about 155 MeV (see Ref. 83), whereas the beam energy per nucleon (c.m.) is 182 MeV/nucleon. At 2.1 GeV/nucleon we assumed that half the available energy goes to the baryon degrees of freedom and the remaining half to the pion degrees of freedom. A justification of this assumption is written in detail in Ref. 86. This value has a large uncertainty but the main argument discussed in the text is not largely affected by this uncertainty. At 400 MeV/nucleon the uncertainty of the value of the horizontal axis is negligibly small.

by Mishustin *et al.* It should be noted that the entropy value also strongly depends on the nuclear matter density, as pointed out in Refs. 83 and 85, so that the discrepancy between the theory and experiment at 400 MeV/nucleon might simply imply that composite fragments are emitted at the stage when the nucleon density is very small (such as $\rho/\rho_0 \sim 0.2$). Another possibility, which was pointed out very recently by Stöcker,[87] is that the quantity of entropy may not be directly related to the d/p ratio. According to him, the hydrodynamical-thermal model which takes into account the shock compression gives a value of $-\ln(N_d/N_p)$ around 0.9 to 1.6; thus, the value of the right-hand side of Eq. (41) is almost independent of the beam energy. On the other hand, the entropy value has a strong beam-energy dependence. Therefore, his conclusion is that the entropy is not related to the d/p ratio in the form of Eq. (41). A preliminary result from his calculations is shown in Fig. 39. These calculations reproduce our observed d/p and π^-/Z ratios very well.

One of the interesting questions regarding the entropy is whether it is constant during the collision processes; if so, it tells us some useful information about the equation of state in the early stage of the collisions. However, according to the recent theoretical work by Csernai and Barz,[88] this quantity is not necessarily constant. Obviously this is an interesting question for the future. Furthermore, the entropies studied from ^{3}H, ^{3}He, and ^{4}He spectra also form an interesting future subject.

VII. SUMMARY

As mentioned in Sec. I, a high-energy nuclear collision may be regarded as a superposition of nucleon-nucleon collisions, and, consequently, the participant-spectator idealization is expected to hold reasonably well. In the present experiment the total nuclear charge yields have been studied, and are very well explained by this picture.

From the plot of the proton invariant cross sections in the $y - p_T/m_pc$ plane we have learned that the effects of projectile and target fragmentations are separable in the small p_T region, while in the large p_T region both projectile and target contributions are highly intermingled.

The energy distributions of protons emitted at c.m. 90° are characterized by a shoulder-arm type of spectrum shape with an exponential falloff at high energies, whereas the energy spectra of pions at the same angle are of a nearly exponential type over the entire range of energy measured in the present experiment. The inverse of the exponential slope, E_0 is systematically larger for protons than for pions. This E_0 is also larger for heavier-mass projectiles and targets. Further, it increases monotonically with the beam energy, and at high energies E_0 seems to approach the limiting value of about 140 MeV for protons and about 120 MeV for pions. These features of E_0 tell us that in the transverse direction the average kinetic energy of protons is larger than that of pions, and that the energy transfer in this direction during the collision is larger for heavier-mass projectile and target system and for higher beam energies. The limiting feature of E_0 at high energies indicates that the average energy transfer into the transverse direction does not linearly increase with the available beam energy in the c.m. frame.

At 800 MeV/nucleon, proton and pion emission into the large p_T region has a stronger projectile- and target-mass dependence than does emission into the small p_T region. In addition, in the small p_T region the mass dependence is close to the geometrical limit of $A^{5/3}$. These facts imply that multiple NN collisions are important in the production of large p_T particles. On the other hand, proton emission at forward angles almost follows the $A^{5/3}$ mass dependence up to fairly high momenta (< 2 GeV/c). The high-momentum parts of the spectra at forward angles are thus not necessarily due to multiple NN collisions. Other contributions such as those due to momentum fluctuation of nucleons (Fermi motion) inside the projectile must be considered.

The angular anisotropy in the c.m. frame is larger for protons than for pions. For an 800 MeV/ nucleon beam, the anisotropy of pions reaches its maximum at a pion energy at around 150 MeV. These features have not yet been explained by any conventional model, but it seems that such a feature of pion emission is consistent with the Δ-isobar model, since the decay from delta increases the pion yield at around 150 MeV and might have a large anisotropy there.

Yield ratios of π^- to total nuclear charge have been studied in order to compare the present data with streamer chamber results. Our data for equal-mass collisions agree very well with the central-collision triggered data of Ar + KCl taken by the streamer chamber. The smaller π^- to total nuclear charge ratio for the larger-mass target suggests the importance of pion absorption.

In order to determine the importance of Coulomb effets in inclusive processes we have studied both the

ratio of π^- to π^+ production and that for ^{3}H to ^{3}He. In the small momentum region and especially at forward angles, such as 30°, the π^- to π^+ ratio is significantly larger than the neutron to proton ratio of the system. This strongly suggests the importance of the Coulomb effect for low-energy pion emission at finite angles. The ratio of ^{3}H to ^{3}He is also larger than the neutron to proton ratio of the system, especially in the small momentum region of these fragments. These results may not be due solely to Coulomb effects but may involve other mechanisms related to the formation of composite fragments such as those mentioned in greater detail in Sec. VI B.

The spectrum shape of composite fragments containing A nucleons is explained very well by the Ath power of the observed proton spectra. The measured coalescence coefficients do not depend on the beam energy but only on the projectile and target masses and the fragment type. These facts suggest the importance of final-state interactions in forming the composite fragments. Sizes of the interaction region have been evaluated from the observed coalescence coefficients. They agree with the data of pion interferometry results. In addition, we observe that the size is smaller for the emission of heavier mass fragments.

The yield ratio of composite fragments to protons strongly depends on the projectile and target masses and the beam energy. However, this ratio does not depend on the emission angle of the fragments. We have also studied the concept of entropy, especially the problem of the large discrepancy between the experimental and theoretical values, which has been pointed out by Siemens and Kapusta. Within the present analysis, such a discrepancy is not observed with 800 and 2100 MeV/nucleon beams, but only with 400 MeV/nucleon beams.

In the present paper we have also compared the data with theoretical models. Both the thermal and single NN collision models have succeeded in reproducing some of the gross features observed in the data. However, these models have many difficulties in reproducing the detailed structures seen in the data. In general, models that are classified with either the thermal model or single NN collision model succeed in reproducing certain aspects of the data on one hand, while on the other hand, they fail to reproduce others. For example, the isentropic expansion model has succeeded in reproducing the slope difference between protons and pions as well as the shoulder-arm spectrum shape of protons, but has failed in reproducing the pion yields. In this regard the unified models described in Sec. VI F 3. are better in reproducing the data and perhaps should be developed more extensively in the future.

We conclude the paper by mentioning that the present data of inclusive spectra have revealed several features that are unique to high-energy nuclear collisions. Although most of these features can qualitatively be explained in terms of nonexotic orthodox theories, none of the currently available theories have a full quantitative explanation of all the observed data presented here.

ACKNOWLEDGMENTS

The present measurements have been carried out at the Bevatron/Bevalac at the Lawrence Berkeley Laboratory. We acknowledge with thanks the important role played in this work by the Bevatron and Hilac crews, especially in their expert operation of the machine. Our special thanks go to O. Chamberlain for his continuous encouragement throughout this work and to R. Fuzesy for his excellent technical support at various stages of the experiment. Stimulating discussion with J. Randrup and M. Gyulassy are gratefully acknowledged. One of us (E.M.) thanks the Deutsche Forschungsgemeinschaft for its financial support. This work was supported by the Director of the Office of Energy Research, Division of Nuclear Physics of the Office of High-Energy and Nuclear Physics of the U. S. Department of Energy under Contract W-7405-ENG-48. It was also supported by the INS-LBL Collaboration Program and a grant from the Commemorative Association of the Japan World Exposition.

---

*Present address: DPhN/ME, CEN de Saclay, 91190 Gif-sur-Yvette, France.

†Present address: Institut for Theoretische Physik, Freie Universität Berlin, 1000 Berlin 33, West Germany.

‡Present address: Institute for Nuclear Study, University of Tokyo, Tanashi-shi, Tokyo, Japan.

[1]S. Nagamiya, I. Tanihata, S. Schnetzer, L. Anderson, W. Brückner, O. Chamberlain, G. Shapiro, and H. Steiner, J. Phys. Soc. Jpn. Suppl. 44, 38 (1978).

[2]S. Nagamiya, L. Anderson, W. Brückner, O. Chamberlain, M. -C. Lemaire, S. Schnetzer, G. Shapiro, H. Steiner, and I. Tanihata, Phys. Lett. 81B, 147 (1979).

[3]M. -C. Lemaire, S. Nagamiya, S. Schnetzer, H. Steiner, and I. Tanihata, Phys. Lett. 85B, 38 (1979).

[4]I. Tanihata, S. Nagamiya, O. Chamberlain, M. -C. Lemaire, S. Schnetzer, G. Shapiro, and H. Steiner, Phys. Lett. 87B, 349 (1979).
[5]S. Nagamiya, M. -C. Lemaire, S. Schnetzer, H. Steiner, and I. Tanihata, Phys. Rev. Lett. 45, 602 (1980).
[6]I. Tanihata, M. -C. Lemaire, S. Nagamiya, and S. Schnetzer, Phys. Lett. 97B, 363 (1980).
[7]I. Tanihata, S. Nagamiya, S. Schnetzer, and H. Steiner, Phys. Lett. 100B, 121 (1981).
[8]J. Papp, J. Jaros, L. Schroeder, J. Staples, H. Steiner, A. Wagner, and J. Wiss, Phys. Rev. Lett. 34, 601 (1975); J. Papp, Lawrence Berkeley Laboratory Report LBL-3633, 1975.
[9]L. Anderson, Lawrence Berkeley Laboratory Report LBL-6767, 1977.
[10]D. E. Greiner, P. J. Lindstrom, H. Heckman, B. Cork, and F. S. Bieser, Phys. Rev. Lett. 35, 152 (1975).
[11]P. J. Lindstrom, D. E. Greiner, H. Heckman, B. Cork, and F. S. Bieser, Lawrence Berkeley Laboratory Report LBL-3650, 1975 (unpublished).
[12]H. Heckman, D. E. Greiner, P. J. Lindstrom, and H. Shwe, Phys. Rev. C 17, 1735 (1978).
[13]G. D. Westfall, L. D. Wilson, P. J. Lindstrom, H. J. Crawford, D. E. Greiner, and H. H. Heckman, Phys. Rev. C 19, 1309 (1978).
[14]M. M. Gazzaly, J. B. Carroll, J. V. Geaga, G. Igo, J. B. McClelland, M. A. Nasse, H. Spinka, A. L. Sagle, V. Perez-Mendez, R. Talaga, E. T. B. Whipple, and F. Zarbakhsh, Phys. Lett. 79B, 325 (1978).
[15]L. S. Schroeder, S. A. Chessin, J. V. Geaga, J. Y. Grossiord, J. W. Harris, D. L. Hendrie, R. Treuhaft, and K. Van Bibber, Phys. Rev. Lett. 43, 1787 (1979).
[16]G. D. Westfall, J. Gosset, P. J. Johansen, A. M. Poskanzer, W. G. Meyer, H. H. Gutbrod, A. Sandoval, and R. Stock, Phys. Rev. Lett. 37, 1202 (1976).
[17]H. H. Gutbord, A. Sandoval, P. J. Johansen, A. M. Poskanzer, J. Gosset, W. G. Meyer, G. D. Westfall, and R. Stock, Phys. Rev. Lett. 37, 667 (1976).
[18]J. Gosset, H. H. Gutbrod, W. G. Meyer, A. M. Poskanzer, A. Sandoval, R. Stock, and G. D. Westfall, Phys. Rev. C 16, 629 (1977).
[19]R. Stock, H. H. Gutbrod, W. G. Meyer, A. M. Poskanzer, A. Sandoval, J. Gosset, C. H. King, G. King, Ch. Luckner, Nguyen Van Sen, G. D. Westfall, and K. L. Wolf, Phys. Rev. Lett. 44, 1243 (1980).
[20]A. Sandoval, H. H. Gutbrod, W. G. Meyer, R. Stock, Ch. Luckner, A. M. Poskanzer, J. Gosset, J. -C. Jourdain, C. H. King, G. King, Nguygen Van Sen, G. D. Westfall, and K. L. Wolf, Phys. Rev. C 21, 1321 (1980).
[21]J. Chiba, K. Nakai, I. Tanihata, S. Nagamiya, H. Bowman, J. Ingersoll, and J. O. Rasmussen, Phys. Rev. C 20, 1332 (1979).
[22]K. Nakai, J. Chiba, I. Tanihata, M. Sasao, H. Bowman, S. Nagamiya, and J. O. Rasmussen, Phys. Rev. C 20, 2210 (1979).
[23]K. L. Wolf, H. H. Gutbrod, W. G. Meyer, A. M. Poskanzer, A. Sandoval, R. Stock, J. Gosset, C. H. King, G. King, Nguyen Van Sen, and G. D. Westfall, Phys. Rev. Lett. 42, 1448 (1979).
[24]W. Benenson, G. Bertsch, G. M. Crawley, E. Kashy, J. A. Nolen, Jr., H. Bowman, J. G. Ingersoll, J. O. Rasmussen, J. Sullivan, M. Koike, J. Peter, and T. E. Ward, Phys. Rev. Lett. 43, 683 (1979).
[25]E. Moeller, M. -C. Lemaire, S. Nagamiya, S. Schnetzer, H. Steiner, and I. Tanihata, Lawrence Berkeley Laboratory Report LBL-12257, 1981.
[26]O. Bohigas and S. Stringari, Phys. Lett. 95B, 9 (1980).
[27]T. Fujita and J. Jüfner, Nucl. Phys. A343, 493 (1980).
[28]A. M. Baldin, N. Giordenescu, V. N. Zubarev, L. K. Ivanova, N. S. Moroz, A. A. Povtoreiko, V. B. Radomanov, and V. S. Stavinskii, Yad. Fiz. 20, 1201 (1975) [Sov. J. Nucl. Phys. 20, 629 (1976)]; A. M. Baldin, in *High Energy Physics and Nuclear Structure—1975 (Santa Fe and Los Alamos)*, Proceedings of the Sixth International Conference on High Energy Physics and Nuclear Structure, edited by D. E. Nagle and A. S. Goldhaber (AIP, New York, 1975), p. 620.
[29]S. Frankel, Phys. Rev. Lett. 38, 1338 (1977).
[30]V. V. Burov, V. K. Lukyanov, and A. I. Titov, Phys. Lett. 67B, 46 (1977).
[31]Y. D. Bayukov, V. I. Efremenko, S. Frankel, W. Frati, M. Gazzaly, G. A. Leskin, N. A. Nikiforov, C. F. Perdrisat, V. I. Tchistilin, and Y. M. Zaitsev, Phys. Rev. C 20, 764 (1979).
[32]Theoretical aspects of the backward production have been studied by a number of authors; see, for example, T. Fujita and J. Hüfner, Nucl. Phys. A314, 317 (1979), and references therein.
[33]J. D. Bowman, W. J. Swiatecki, and C. F. Tsang, Lawrence Berkeley Laboratory Report LBL-2908, 1973 (unpublished).
[34]R. J. Glauber and G. Matthiae, Nucl. Phys. B21, 135 (1970).
[35]J. Hüfner and J. Knoll, Nucl. Phys. A290, 460 (1977); also see J. Hüfner, in Proceedings of the 4th High-Energy Heavy-Ion Summer Study, Berkeley, 1978, Lawrence Berkeley Laboratory Report LBL-7766, p. 135.
[36]Some readers may worry about the effects of the projectile fragments for particle emission at forward angles. For A on A collisions with $N = Z = A/2$ a simple participant-spectator model based on the straight-line geometry leads to an A dependence of the nuclear charge yields of projectile fragments, which is given by (see Ref. 37) $Y^{\text{proj frag}}(\text{nuclear charge}) = (\frac{3}{2})\pi r_0^2 A^{5/3}$. This formula agrees reasonably well with the observed data (see Ref. 37). It should be compared with the A dependence of the nuclear charge yields of the participant region, $Y^{\text{parti}}(\text{nuclear charge}) = \pi r_0^2 A^{5/3}$, which can easily be derived from Eq. (9). The A dependence for both cases is the same. Currently it is not known if the A dependence of the *proton yields* is the same as that of the *nuclear charge yields* for projectile fragments. Nevertheless, we can see from the comparison

of the above two formulas that it is not easy to extract any effect due to the mixture of the projectile fragments into the participant nucleons from a study of the A dependence alone.

[37]S. Nagamiya, Nucl. Phys. A335, 517 (1980).

[38]J. Gosset, J. I. Kapusta, and G. D. Westfall, Phys. Rev. C 18, 844 (1978).

[39]R. L. Hatch and S. E. Koonin, Phys. Lett. 81B, 1 (1978).

[40]V. G. Antonenko, V. M. Galitskij, Yu. I. Grigor'yan, M. S. Ippolitov, K. V. Karadjev, E. A. Kuz'min, V. I. Manko, A. A. Ogloblin, V. V. Paramonov, A. A. Tsvetkov, and A. A. Vinogradov, Institute of Atomic Energy Report IAE-3220, 1979.

[41]S. Frankel, University of Pennsylvania Report UPR-0087, 1978 (unpublished).

[42]S. Y. Fung, W. Gorn, G. P. Kiernan, F. F. Liu, J. J. Lu, Y. T. Oh, J. Ozawa, and R. T. Poe, Phys. Rev. Lett. 40, 292 (1978).

[43]A. Sandoval, R. Stock, H. E. Stelzer, R. E. Renfordt, J. W. Harris, J. P. Branniggan, J. V. Geaga, L. J. Rosenberg, L. S. Schroeder, and K. L. Wolf, Phys. Rev. Lett. 45, 874 (1980).

[44]K. G. Libbrecht and S. E. Koonin, Phys. Rev. Lett. 43, 1581 (1979).

[45]M. Gyulassy and S. K. Kauffmann, Nucl. Phys. A362, 503 (1981).

[46]M. Gyulassy, private communication.

[47]Recent review of thermal models is given by S. Das-Gupta and A. Z. Mekjian, Phys. Rep. (in press).

[48]M. Sobel, P. J. Siemens, J. P. Bondorf, and H. A. Bethe, Nucl. Phys. A251, 502 (1975).

[49]A. Z. Mekjian, Nucl. Phys. A312, 491 (1978); Phys. Rev. Lett. 38, 604 (1977); Phys. Rev. C 17, 1051 (1978).

[50]J. I. Kapusta, Phys. Rev. C 16, 1493 (1977).

[51]W. D. Myers, Nucl. Phys. A296, 177 (1978).

[52]S. DasGupta, Phys. Rev. Lett. 41, 1450 (1978).

[53]P. J. Siemens and J. O. Rasmussen, Phys. Rev. Lett. 42, 880 (1979).

[54]J. I. Kapusta and D. Strottman, Phys. Rev. C 23, 1282 (1981).

[55]I. A. Schmidt and R. Blankenbecler, Phys. Rev. D 15, 3321 (1977).

[56]S. J. Lindenbaum and R. M. Sternheimer, Phys. Rev. 105, 1874 (1957).

[57]T. P. Clemente and L. Winsberg, Lawrence Radiation Laboratory Report UCRL-9043, 1960 (unpublished).

[58]H. J. Pirner and B. Schürmann, Nucl. Phys. A316, 461 (1979).

[59]R. Malfliet, Phys. Rev. Lett. 44, 864 (1980).

[60]M. Chemtob and B. Schürmann, Nucl. Phys. A336, 508 (1980).

[61]J. Randrup Phys. Lett. 76B, 547 (1978).

[62]J. Knoll and J. Randrup, Nucl. Phys. A324, 445 (1979).

[63]J. Knoll, Phys. Rev. C 20, 773 (1979).

[64]S. Bohrmann and J. Knoll, Nucl. Phys. A356, 498 (1981).

[65]A. R. Bodmer, C. N. Panos, and A. D. MacKeller, Phys. Rev. C 22, 1025 (1980).

[66]D. J. E. Callaway, L. Wilets, and Y. Yariv, Nucl. Phys. A327, 250 (1979).

[67]R. K. Smith and M. Danos, private communication.

[68]K. K. Gudima, H. Iwe, and V. D. Toneev, J. Phys. G 5, 229 (1979).

[69]J. D. Stevenson, Phys. Rev. Lett. 41, 1702 (1978).

[70]Y. Yariv and Z. Fraenkel, Phys. Rev. C 20, 2227 (1979).

[71]J. Cugnon, Phys. Rev. C 22, 1885 (1980).

[72]S. F. Butler and C. A. Pearson, Phys. Rev. 129, 836 (1963).

[73]A. Schwarzschild and C̃. Zupancĩc̃, Phys. Rev. 229, 854 (1963).

[74]In the low-energy region the observed neutron spectra are different from the proton spectra (see Ref. 75). However, in most of the energy region dealt with in the present paper, we can approximate $\sigma_I(p) = \sigma_I(n)$.

[75]W. Schimmerling, J. Kast, D. Ortehdahl, R. Madey, R. A. Cecil, B. D. Anderson, and A. R. Baldwin, Phys. Rev. Lett. 43, 1985 (1979).

[76]J. I. Kapusta, Phys. Rev. C 21, 1301 (1980).

[77]A. S. Goldhaber and H. H. Heckman, Annu. Rev. Nucl. Part. Sci. 28, 161 (1979).

[78]S. Y. Fung, W. Gorn, G. P. Kiernan, J. J. Lu, Y. T. Oh, and R. T. Poe, Phys. Rev. Lett. 41, 1592 (1978).

[79]H. Sato and K. Yazaki, Phys. Lett. 98B, 153 (1981).

[80]R. Bond, P. J. Johansen, S. E. Koonin, and S. Garpman, Phys. Lett. 71B, 43 (1977).

[81]J. Randrup and S. E. Koonin, Nucl. Phys. A356, 223 (1981).

[82]J. D. Stevenson, Phys. Rev. Lett. 45, 1773 (1980).

[83]P. J. Siemens and J. I. Kapusta, Phys. Rev. Lett. 43, 1486 (1979); 43, 1690 (1979) (E).

[84]I. N. Mishustin, F. Myhrer, and P. J. Siemens, Phys. Lett. 95B, 361 (1980).

[85]S. I. A. Garpman, N. K. Glendenning, and Y. J. Karant, Nucl. Phys. A322, 382 (1979).

[86]This assumption is very crude. However, as we see from Table V, for 2.1 GeV/nucleon beams about half the energy flux emerges in the form of pions (π^-,π^0, and π^+) while the remaining half is in the form of nucleons (p and n) and composite fragments. Therefore, this assumption is not too unreasonable.

[87]H. Stöcker, Lawrence Berkeley Laboratory Report LBL-12302, 1981 (unpublished), and also private communication.

[88]L. P. Csernai and H. W. Barz, Z. Phys. A 296, 173 (1980).